



**Politecnico
di Torino**

Politecnico di Torino

Dipartimento di Ingegneria Energetica
Corso di Laurea Magistrale in Ingegneria Energetica e Nucleare
Sessione di Laurea Marzo 2023

Tesi di Laurea Magistrale

Modelling and integration of Power- to-X systems in electric grids with high renewable energy production

Relatore:
Prof. Raffaele Pirone

Candidato:
Antonio De Gennaro

Correlatori:
Ing. Fabio Salomone
Ing. Andrea Mazza

Anno accademico 2022/2023

Summary

With the increasing diffusion of the Renewable Energy Storage (RES), aimed both at the achievement of the European targets and the reduction of CO₂ fossil emissions, the management of the electric grid is more and more challenging due to the intermittence and variability of the generation sources. In such context, three Power-to-X plant types (methane, methanol and syngas) are considered. They have been installed on an electric grid hosting large share photovoltaic, seeking to evaluate possible impacts and benefits. Both the methanation and the syngas production models have been built taking into account the entire process chain. Conversely, the methanol synthesis plant has been created starting from a model already defined in literature. The simulation span is composed of two weeks: one during January and the other one during June. In general, the simulation outcomes show that the PtX installation leads to a clear reduction of the reverse power flow (RPF) phenomenon. In addition, thanks to the simulations, other two indexes have been calculated: the grid losses and the capacity factors of the installed plants. The results depend on the PtX size, the typology, the number of PtX plants installed and the number of the PV plants considered. Among the three kinds of PtX, the syngas production plants minimise the RPF and maximise the capacity factor, while the power losses are minimised through the installation of methane production plants.

Table of Contents

List of Figures	3
List of Tables.....	5
Nomenclature	6
1. Introduction.....	7
2. Electric grid and renewable energy source	13
2.1 Power System Structure	13
2.2 Grid model	14
2.3 RES generation	16
2.4 PV production	18
2.5 Backward and Forward Sweep Algorithm.....	21
3. Modelling of the Power-to-X processes.....	25
3.1 Electrolyser	27
3.2 Methanation	34
3.3 Methanol synthesis.....	39
3.4 Syngas synthesis	42
3.5 Hydrogen storage	45
3.6 PtX model strategy.....	47
4. Validation and comparison of the of the PtX models	51
5. Cases of study	57
6. Outcomes of the model	63
6.1 Reverse Power Flow	63
6.2 Grid losses.....	65
6.3 Nodal voltage and branch current	67
6.4 Capacity factor	72
6.5 PtX efficiency	78

6.6	Embedded CO ₂ in the product	80
7.	Future studies	83
8.	Conclusion	85
	Appendix	87
	Appendix A - CO ₂ Capture plant	87
	Appendix B – MATLAB code description	88
	References	92
	Acknowledgements	97

List of Figures

Figure 1.1	CO ₂ emission expressed for sectors [2].....	8
Figure 2.1	MV semi-urban grid [12].....	14
Figure 2.2	Renewables share of power generation [16].....	17
Figure 2.3	Renewable power generation by technology [16].....	17
Figure 2.4	Renewable net capacity additions by technology [15].....	18
Figure 2.5	Daily normalised PV profile (reference January).....	20
Figure 2.6	Block diagram of the Backward and Forward Sweep algorithm.....	23
Figure 3.1	Simplified scheme of the PtX plant components.....	25
Figure 3.2	Electrolyser structure (PEMWE).....	27
Figure 3.3	PEMWE cell polarization curve.	31
Figure 3.4	PEMWE hydrogen production as function of power absorbed.	32
Figure 3.5	PEMWE Efficiency	33
Figure 3.6	Electrolyser plant scheme.....	33
Figure 3.7	Methanation plant scheme	36
Figure 3.8	Methanol synthesis plant scheme	41
Figure 3.9	Syngas plant scheme.....	43
Figure 3.10	Hydrogen storage scheme.....	45
Figure 3.11	Normalised number of switch on/off of the FPP for different autonomies ..	46
Figure 3.12	Block diagram of the PtX model strategy	50
Figure 4.1	Power-to-Methane power absorption profile.....	52
Figure 4.2	Power-to-Syngas power absorption profile	52
Figure 4.3	Power-to-Methanol power absorption profile	53
Figure 4.4	Hydrogen storage level – Power-to-Syngas model validation	54
Figure 5.1	Winter power surplus at node 11 for 30% of PV share	59
Figure 5.2	Summer power surplus at node 11 for 30% of PV share	59
Figure 5.3	Winter power surplus at node 11 for 50% of PV share	60
Figure 5.4	Summer power surplus at node 11 for 50% of PV share	60
Figure 6.1	Maximum and minimum voltage profile in winter scenario with 30% of PV share	68

Figure 6.2	Maximum and minimum voltage profile in summer scenario with 30% of PV share	68
Figure 6.3	Maximum and minimum voltage profile in winter scenario with 50% of PV share	69
Figure 6.4	Maximum and minimum voltage profile in summer scenario with 50% of PV share	69
Figure 6.5	Maximum branch load in winter scenario with 30% of PV share.....	70
Figure 6.6	Maximum branch load in summer scenario with 30% of PV share	71
Figure 6.7	Maximum branch load in winter scenario with 50% of PV share.....	71
Figure 6.8	Maximum branch load in summer scenario with 50% of PV share	72
Figure 6.9	PtX capacity factors in winter scenario with 30% of PV share.....	73
Figure 6.10	Hydrogen storage level in winter scenario with 30% of PV share (Power-to-Methane installed at node 11)	75
Figure 6.11	PtX capacity factors in summer scenario with 30% of PV share	76
Figure 6.12	Hydrogen storage level in summer scenario with 30% of PV share (Power-to-Methane installed at node 11).....	77
Figure 6.13	PtX capacity factors in both reference periods (dashed line for the winter and continues line for the summer) with 50% of PV share	78
Figure A.1	CO ₂ capture plant with MEA.....	88
Figure A.2	Block diagram of algorithm implemented through the MATLAB code	90

List of Tables

Table 2.1	Distribution of the load types on the branch length [12]	15
Table 2.2	Total load installed for each type [12]	15
Table 3.1	PEMWE polarization curve parameters [22]	31
Table 5.1	PtX installation nodes and sizes [12]	58
Table 6.1	Reverse Power Flow for 30% of PV share	63
Table 6.2	Reverse Power Flow for 50% of PV share	64
Table 6.3	Grid losses for 30% of PV share	66
Table 6.4	Grid losses for 50% of PV share	67
Table 6.5	FPP night working times per week in winter scenario with 30% of PV share	74
Table 6.6	PtX efficiency for both the PV share and the simulation periods	79
Table 6.7	PtX converted CO ₂ for both the PV share and the simulation periods	81
Table A.1	CO ₂ concentrations of several flue gases [47] [48]	87
Table A.2	Strategy parameters of the model	91

Nomenclature

Acronyms and abbreviations

PtX	Power to X plant
PtG	Power to gas
PtL	Power to liquid
RES	Renewable energy source
GHG	Greenhouse gas
RPF	Reverse power flow
PEMWE	Proton exchanger membrane water electrolysis
LCOE	Levelized cost of energy
CC	Carbon capture plant
RTE	Round trip efficiency
LV	Low voltage
MV	Medium voltage
HV	High voltage
LTE	Low temperature electrolyser
HTE	High temperature electrolyser
MEA	Monoethanolamine
FPP	Final product plant
CF	Capacity factor
ICE	Internal combustion engine

1. Introduction

The so-called Power-to-Gas (PtG) and Power-to-Liquid (PtL) plants, commonly classified into the Power-to-X group, are technologies that enable the conversion of electric energy into chemical one. Their diffusion in the current and, above all, future energy scenario is due to many factors, such as the intrinsic nature of the process, the grid management, and environmental aspects.

The electric grid is developed over the years on the basis of a centralised production system and a unidirect power flow, from generation to consumption. The wide diffusion of Renewable Energy Source (RES) leading to a radical change of the electricity generation, and, indeed, the latter one is becoming more and more decentralised (the energy production plants are installed at distribution level too). This shift is introducing several issues in the management and operation of the grid. Indeed, a high share of RES lead to possible grid issues, like the reverse power flows, higher voltage values, and overloading. Furthermore, since the RES production is intermittent, it could happen that to preserve the stability of the electrical grid (production and demand must be in equilibrium) part of the energy production is curtailed if not storable in other ways. The installation of PtX plants on key nodes of the grid could be considered as an active strategy to limit or, the best case, to completely remove the grid issues and, in addition, to better exploit the RES storing the surplus in chemical stable molecules having high energy potential.

From the environmental view point it is possible to have benefits coupling CO₂ carbon capture plants to PtX. Indeed, hydrogen and carbon dioxide are the two fundamental reactants that, in different process conditions, enable to obtain several useful products. The CO₂ in this way can be sequestered from the environment and reutilised. Nowadays, this aspect cannot be neglected considering that from 1990 to 2019 the global CO₂ emissions increased by 68%, which means that in 2019 around 38 billion of tons of CO₂ were released in the environment [1]. In 2019, most of the CO₂ emitted in Italy are mainly attributable to the combustion of fossil fuels for the transport (30.7%), energy production (26.9%) and not-industrial sectors (22.6%) [2]. The data are reported in *Figure 1.1*.

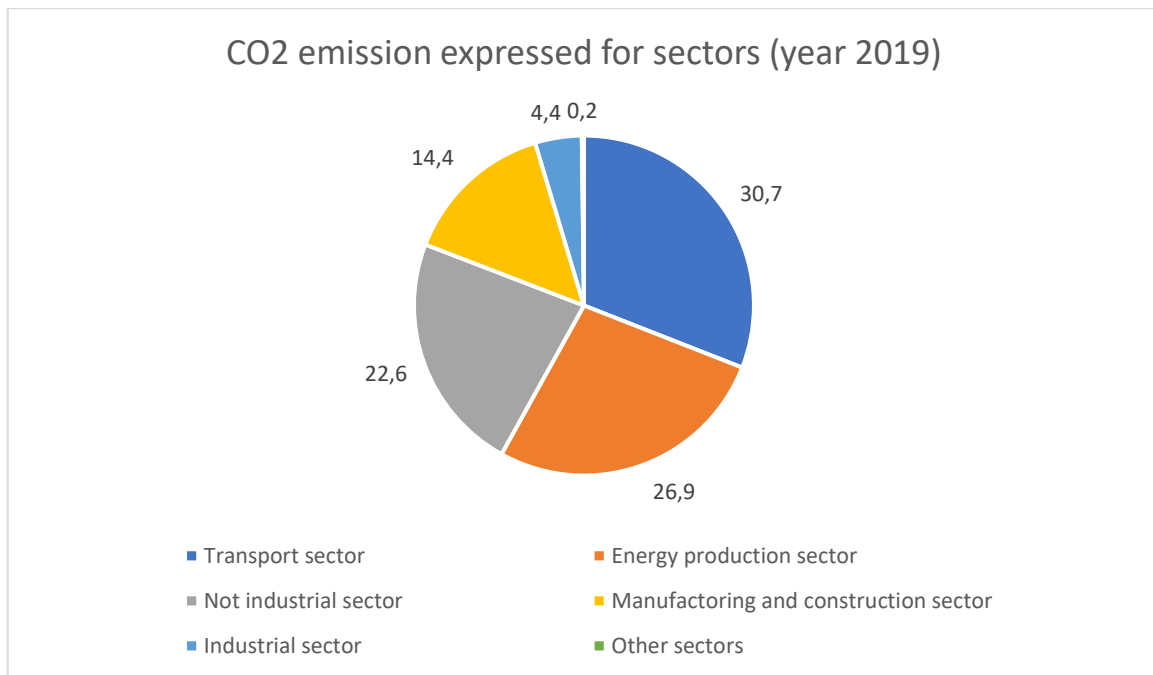


Figure 1.1 CO₂ emission expressed for sectors [2]

The total amount of greenhouse gas (GHG) emitted in Europe in 2019, where the 80% is represented by CO₂, were $4.07 \cdot 10^9$ tonnes. Only a relatively small fraction is attributable to Italy, specifically around 10% ($0.418 \cdot 10^9$ tonnes) [3].

Based on that, several states are working to promote policies that aim at reducing or reaching zero CO₂ emission starting from the Kyoto Protocol in 1998 [4] and then the Paris Agreement in 2015 [5]. In 2019, the EU Member States stipulated the European Green Deal putting forward several goals to accomplish by 2050. Among them, the ‘Fit for 55’ package that the European Commission included to address the climate change and Europe’s carbon neutrality, fixing the target of 40% of renewable energy of the whole energy production by 2030 [6].

So, as suggested from the policies developed and from the aim to reduce the CO₂ emissions, in the short-term and long-term scenarios, a key role of RES, such as photovoltaic and wind plants, in the energy production, is expected. In 2021, RES represented 36% (around 117 GWh) of the Italian gross final electricity consumption [7].

Another aspect to be considered is the possibility to increase the penetration of RES, especially in those sectors hard to electrify or those defined ‘hard-to-abate’, through the installation of PtX plants which allow to obtain ‘green’ chemicals and synthetic fuels.

As all the processes, also the PtX have a conversion efficiency, which is determined by two processes in series. The first efficiency is related to the conversion of the electricity into hydrogen, that vary from 50% to 85% according to the electrolyser technology [8]; the second efficiency is related to the conversion of hydrogen into energetic compounds or vectors considered. Obviously, the global efficiency of the PtX relies strongly on the type of plant deemed.

Besides the PtX plants, in the market there are other electric storage types (besides the PtX plants) like batteries, pumped hydropower storages, flywheels, compressed air storages etc. The main differences among these technologies are related to the charging and discharging time, the amount of energy that can be stored, the maximum storing time, the economic expenditure, and their application fields. Regarding the last aspect, a relevant difference can be detected between the PtX technologies and the others listed. The PtX plants can convert the electricity in chemical energy that usually is used in other sectors and not reinjected back in the electric grid. Instead, the goal of the other storing technologies is to store the energy when there is a surplus from the grid and to partially give it back to electric grid when it is necessary. So, the main storing technologies are related only to the electricity field, while the PtX can couple different energy sectors, like the electric and gas grid. Apart from the advantage reported for the PtX plants, these, if used as the other storing technologies, would result less efficient. As a matter of facts, considering the roundtrip efficiency - the efficiency of the entire charging and discharging process calculated as the ratio between the energy released to the grid during the discharging phase and the energy absorbed during the charging phase - this, related to the PtX plants, assumes moderate values even if highly influenced by the process type. As a general rule, the more the PtX plant implements transformations to obtain the desired product, the less the process will be efficient and, as a consequence, also the possible roundtrip efficiency. For instance, a hydrogen production plant (electrolyser) will be more efficient than a PtX plant that produces methane (in this case, there will be a further conversion step compared to the hydrogen). The RTE for the batteries technologies ranges between 75% and 90%, for the flywheels around 80-90%, for hydro pumped storages is 65-85% and for the compressed air energy storages is 65-75% [9].

As said, it is essential to take into account the context which leads to the diffusion of the PtX, such as:

- High diffusion of RES plants.
- The important goals of capturing and reusing the CO₂ and reducing the GHG emission from fossil fuels to mitigate the effects of climate change and reduce the overall impact of human activities on the environment.
- The possibility of take advantage of the fast response of the electrolyser to follow promptly the surplus power from the grid, limiting the grid management issues.
- The possibility to store the power surplus for, eventually, long period into chemical forms.

Defined the background which would lead to the possible PtX diffusion, the topics addressed in this dissertation are subdivided into next chapters as follows.

The electric grid basic concepts are the first topic discussed in chapter 2. Then the implemented MV grid of the model and the PV generation profile utilised are described. The last aspect dealt with is the description of the algorithm able to solve and obtain the electrical grid working parameters.

Chapter 3 describes in detail the working principle of electrolysers and the model implemented for the consumption evaluation of a Proton Exchanger Membrane Water Electrolysis (PEMWE). This section also conveys and comments the scheme of the three Final Product Plants (FPP). Furthermore, there is a discussion about the autonomy of the hydrogen storage and how it is modelled. At the end of this chapter, a detailed analysis of the considered strategy for the PtX models is reported.

The following part is dedicated to a simulation performed to validate the models proposed and the goodness of the results. Moreover, the main differences between the PtX models are pointed out.

In chapter 5, the case studies are described, specifically, for each simulation, the changed parameters are the reference interval, the Power-to-X typology, and the PV penetration factor.

The chapter 6 shows the outcomes of the grid simulation with and without the installation of PtX. In addition, the different PtX results are compared and analysed in depth.

The next one gathers some ideas that have not been deeply examined in this dissertation, still they would be thought-provoking for future studies.

The dissertation ends by drawing the conclusions and summarising the results.

2. Electric grid and renewable energy source

In this chapter, a briefly overview of the current electric grid status and of the main RES development is offered. In addition, both the electric grid structure and PV generation implemented in the model are described.

2.1 Power System Structure

The power system is composed of three sectors:

- Generation including the different kind of generators [Photovoltaic plant (PV), gas turbine, steam turbine, wind turbine, etc] producing energy usually at Low Voltage (LV, lower than 1kV)/Medium Voltage (MV , from 1 kV to 30 kV) level.
- Transmission, whose goal is to transfer high amount of energy for long distances, with low losses. It is operated at High Voltage (HV), i.e. 220/380 kV. Usually, a HV grid is meshed to ensure the reliability and the resilience of the system.
- Distribution. There are two distribution grid typologies. One representing the grid working at MV level fed by the HV/MV transformers or MV generators. The aim of this grid is to distribute the energy coming from the transmission level to MV/LV transformer usually located close to the loads. In addition, big consumers as factories can be supplied directly by the distribution grid. Usually, it has a weakly meshed structure.

The other representing the grid working at LV fed by MV/LV transformers or LV generators. The utilization grid has as goal the capillary distribution of the energy at the smaller consumer. It has a radial structure.

In the last decades, the distribution electric grids have been subjected to a strong expansion due to the increase of the distributed energy resources installed, that is the energy production near the places in which it is used.

The rapid DER growth has been favoured by multiple factors, such as: the cost reduction of some renewable generators and the promotion of public incentives on a few technologies (like photovoltaic one). The diffusion of the renewable energy production favoured the development of micro-grids interconnected with each other and linked to a larger power grid, leading at an improvement of the energy supply service. Besides the positive aspects, the increase of the distributive generation represents a challenge for the Distribution System

Operators which, in fact, have to manage ever more difficult scenarios. The complexity of the grid is due to the fact that the DER installed in the MT/BT distribution systems could transform the grids from passive to active. This implies both a modification of the original structure and their management.

2.2 Grid model

The grid structure implemented in the model can be classified as a MV distribution grid and it is the result of a European report whose authors collected data from many relevant European DSOs [10]. The distribution grid output parameters of the report are then considered as inputs of Reference Network Model obtaining samples of distribution grid [11]. The sample of the distribution grid considered in the simulations is already the subject of a previous study [12]. Its structure is reported in *Figure 2.1*.

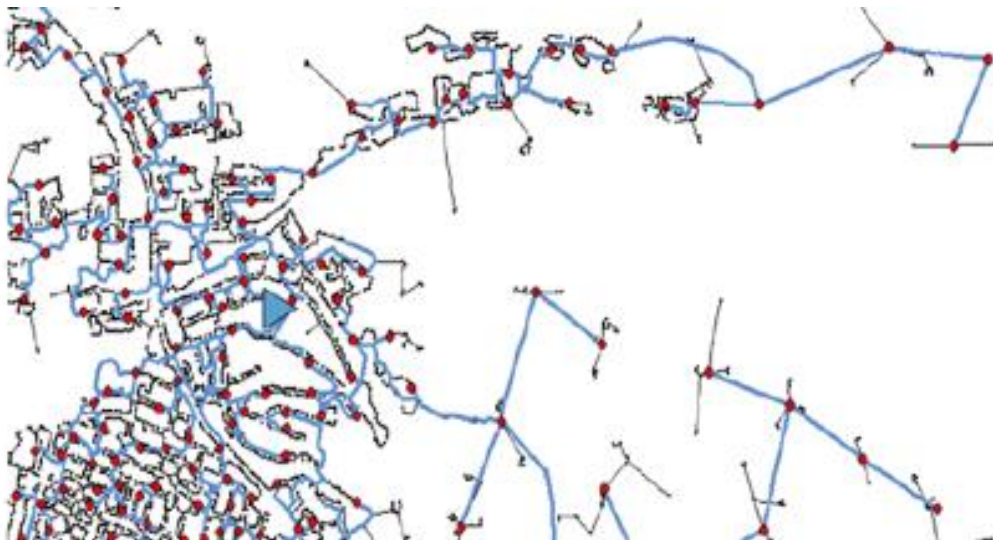


Figure 2.1 MV semi-urban grid [12]

The distribution grid can be classified as a radial semi-urban grid. The absence of loops simplifies the calculation of the power flow inside each branch. The grid consists of 202 MV nodes fed by a HV/MV transformer and 5498 LV nodes. It is assumed that the LV nodes are aggregated as the equivalent load to the nearest MV node. Each branch that links two MV nodes of the distribution grid can be schematised with a π model characterised by four parameters:

- Branches length (L) expressed in km.

- Resistance, it is a longitudinal parameter of the distribution line model that depends on the electrical resistivity of the cable. It is expressed in π/km .
- Inductance, it is expressed in π/km and represents a second longitudinal parameter. It takes into account the auto and mutual induction between the cables; its value depends on the disposition and on the type of cables.
- Susceptance, it is a transversal parameter of the model. It takes into account the electrostatic interaction between the cables and the terrain. In a MV grid this parameter can be neglected.

Moreover, to represents a more realistic scenario, according to the previous study [12], the loads are modified and differentiated on five types: residential, industrial, tertiary, commercial, agricultural. The positioning of the different loads is dependent to length of the branches (*Table 2.1*). The loads are divided as shown in the *Table 2.2*.

Table 2.1 Distribution of the load types on the branch length [12]

Branches length (km)	Residential (%)	Industrial (%)	Tertiary (%)	Commercial (%)	Agricultural (%)
L \leq 0.150	80	0	10	10	0
0.150<L \leq 0.300	70	0	15	15	0
0.300<L \leq 0.500	65	5	15	15	0
0.500<L \leq 0.800	25	5	20	45	5
0.800<L \leq 1.0	10	50	5	25	10
1.0<L \leq 3.5	20	10	5	5	60

Table 2.2 Total load installed for each type [12]

Residential (MW)	Industrial (MW)	Tertiary (MW)	Commercial (MW)	Agricultural (MW)
40	3.5	10.5	14	2.5

2.3 RES generation

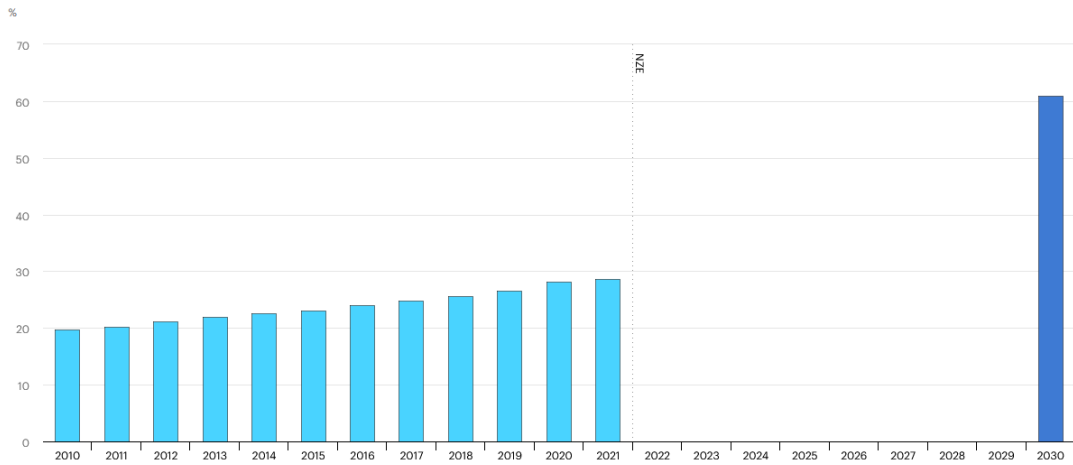
The RES generation means any type of renewable resource that is used to generate electrical energy such as wind, solar, and geothermal generation. Renewable energy is energy derived from natural sources that are replenished at a higher rate than they are consumed.

In the last years the renewables are spreading more and more, and this is due to the following driving forces:

- Key role in clean energy transitions.
- Reduction of technology purchasing cost.
- Reduction of the LCOE.

Their fundamental value in the energy transition field, is spotlighted both along the European Union policies and, also, globally. For what concern the purchasing cost, it can be highlighted that PV modules had paramount reductions along the years. In particular, according to global statistical data, the PV cost per kW peak installed went from 4808 USD/kW in 2010 to 857 USD/kW in 2021, representing a reduction of around 80% of the initial cost [13]. This leads also to a LCOE reduction. The LCOE is an economic index that represents the current cost of the energy produced by the plant, expressed as the ratio between the total plant cost and the total energy produced. This value in 2019, for the PV technology was 0.0680 USD/kWh. For the same reference year, the offshore wind LCOE was 0.1150 USD/kWh, while for the onshore wind was 0.0530 USD/kWh [14].

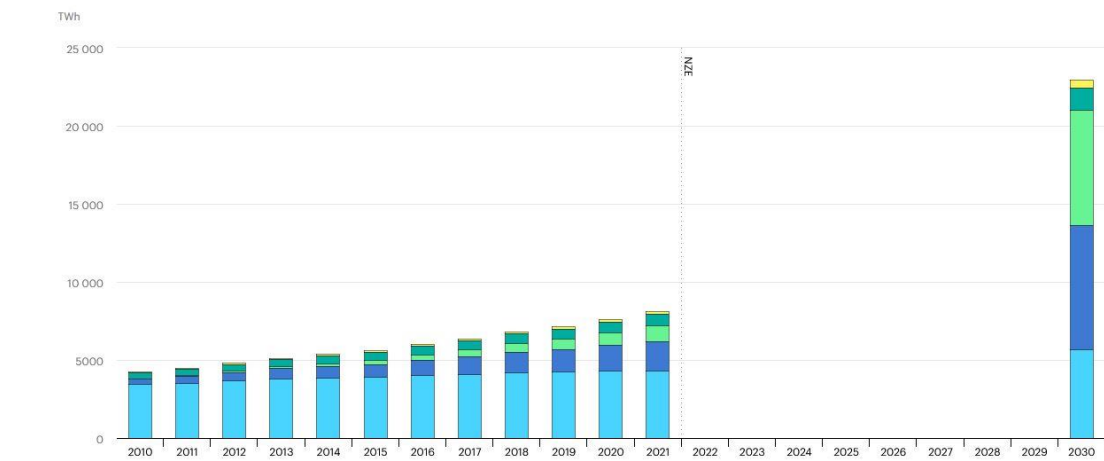
As reported by the International Energy Agency “in 2021 renewable electricity generation rose by almost 7%, a record 522 TWh increase, with wind and solar PV technologies together accounting for almost 90% of this growth. The share of renewables in global electricity generation reached 28.7% in 2021, after modest growth of 0.4 percentage points” [15]. The renewable electricity shares in the last years together with the 2030 goal is reported in *Figure 2.2*.



IEA, Licence: CC BY 4.0

Figure 2.2 Renewables share of power generation [16]

It is also interesting to look in detail the data reported in *Figure 2.3*, where the entire renewable energy production is differentiated by technology. More than half of the share is represented by the hydropower generation. Then there is the wind generation with around 23% of the total RES production. It is followed by the PV generation with a share of 12%, then the bioenergy with slightly more than 9% of share. The other RES, as the wave energy production, cover the remaining part of the production.



IEA, Licence: CC BY 4.0

Hydropower Wind Solar PV Bioenergy Other

Figure 2.3 Renewable power generation by technology [16]

To conclude this general overview of the current renewable energy status, the renewable energy net capacity additions from the 2019 to 2021 are shown in *Figure 2.4*.

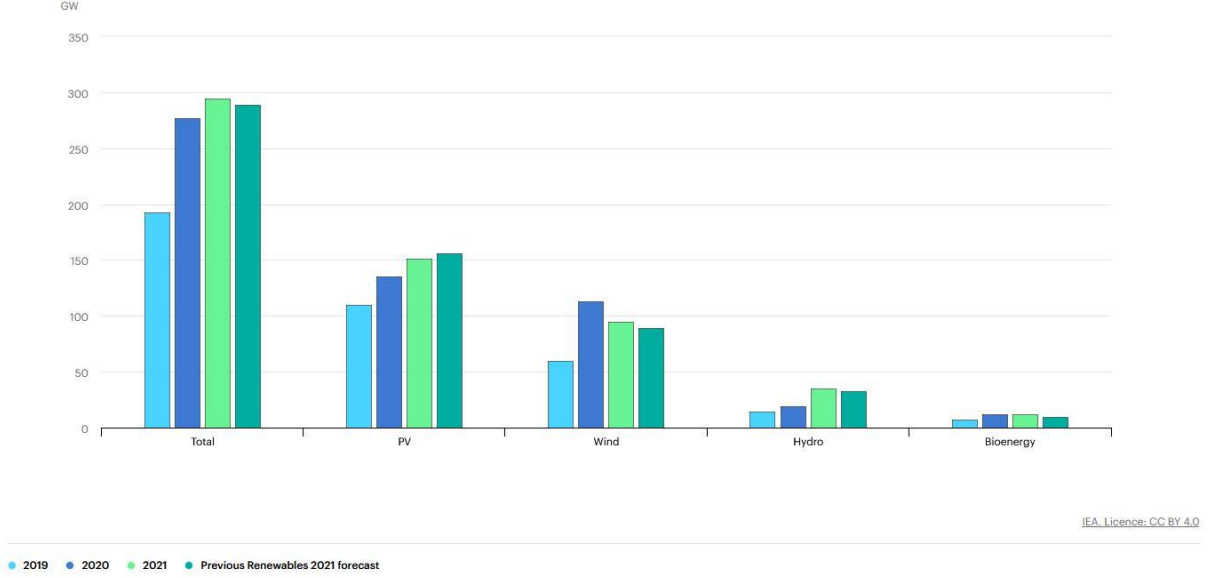


Figure 2.4 Renewable net capacity additions by technology [15]

The graph shows that the total installed power of renewable sources increased from 2019 to 2021. As regards the technologies evaluated in the graph, this trend is not always valid. In fact, only the photovoltaic and hydroelectric sectors have had a constant increase in the installed power. As far as the wind energy production is concerned, in 2021 there was a decrease in the installed power compared to the previous year.

2.4 PV production

The RES considered as generation source in this model is the photovoltaic. Knowing the geographical location, the first step performed is the collection of irradiance data (G) from the BrightModel, an open-source PV simulator [17]. Then, the air temperature (T_{air}) can be obtained from PVGIS website [18]. So, the PV cell working temperature can be evaluated as shown in *Equation 2.1*.

$$T_{cell} = T_{air} + \frac{NOCT - T_{std}}{G_{std}} \cdot G \quad (2.1)$$

where $NOCT$ is the normal operating cell temperature, T_{std} is the standard ambient temperature and G_{std} the standard irradiance evaluated at an air mass coefficient of 1.5.

The thermal efficiency is evaluated in *Equation 2.2*.

$$\eta_{thermal} = 1 + \gamma_{thermal} \cdot (T_{cell} - 25^{\circ}C) \quad (2.2)$$

where $\gamma_{thermal}$ is the thermal coefficient of maximum power.

Introducing η_{AC-DC} as the efficiency that takes into account the inverter and connection losses, the normalised PV production can be calculated as in *Equation 2.3*.

$$\frac{P_{ac}}{P_{nom}} = \eta_{AC-DC} \cdot \eta_{thermal} \cdot \frac{G}{G_{nom}} \quad (2.3)$$

This analysis is performed for the city of Solothurn, where the electric grid of the model is located. Since the area of installation considered is relatively small, it is assumed that all the PV plants installed have the same normalised PV production profile. The power produced by each PV plant installed on the grid is evaluated as the product of the normalised PV power production for the nominal PV power installed.

The useful parameters set to evaluate the PV production are reported in *Table 2.3*.

Table 2.3 PV generation profile parameters [12]

Variables and constants	Value
GPS coordinates	47° 12' 31.805" N 7° 31' 56.248" E
Altitude (m)	432
Tilt angle (°)	35
Azimuth angle (°)	0
Reference months	January / April / July / October
Average month temperature [18] (°C)	-0.1/ 9.2/ 18.2 / 11.5
T_{std} (°C)	20
NOCT (°C)	45
G_{std} (W/m ²)	800
$\gamma_{thermal}$ (°C ⁻¹)	-0,0045
η_{AC-DC} (%)	83
G_{nom} (W/m ²)	1000

The resulting PV profile normalized to the incoming irradiance is show in *Figure 2.5*.

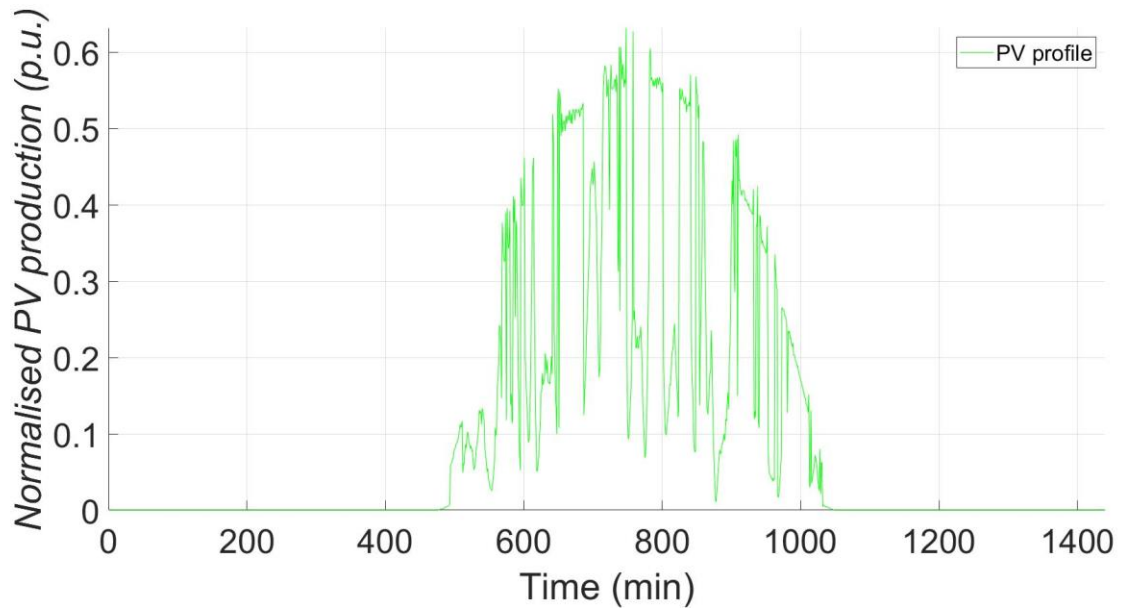


Figure 2.5 Daily normalised PV profile (reference January)

The amount of PV power installed on a grid has pros and cons. To quantify the impact of the PV generation, or in general of the renewable energy sources, the penetration factor has to be introduced. In this study, since the renewable generation source considered is the photovoltaic one, the PV penetration factor is defined. It represents the ratio between the amount of energy supplied by the PV and the total absorbed power by the loads.

If the power supplied by PV plants compared to the whole power supplied is small or moderate, a reduction of both power losses and voltage drop can be observed. If the PV plants have a relevant role in the total power supplied, some issues as the RPF, overloading, and overvoltage, can be detected.

The RPF is a phenomenon that occurs when the power flow at transformer level is inverted. In our case, this happens when the power is sent from the distribution grid to the transmission one. This cause two main issues to the Transmission System Operator (TSO) and Distribution System Operator (DSO). The first is that the node, at which the power is injected in the transmission lines, acts like an active generator not controllable from the TSO. The second issue is related to the protection setting that could be inappropriate RPF. The most common ways to solve this problem are the cutting of the RES production or the storing of the surplus power.

The overvoltage phenomenon occurs when there is an important nodal power injection. The nodal voltage must be within the limit imposed by CEI EN 50160 set to $0.9 \text{ p.u.} \leq V \leq 1.1 \text{ p.u}$ with respect to the nominal voltage. [19].

The overloading phenomenon occurs when the power flowing in a branch is higher than the branch thermal limit. The currents transferred along the grid, in normal operating condition, must be lower than the line thermal limit. For very short time periods, the currents are allowed to exceed the line thermal limit, even though this can affect their life.

In this study, the attention is focused on the RPF. In particular, it will be deepened if and how much the installation of different type of PtX affect this phenomenon.

2.5 Backward and Forward Sweep Algorithm

Once defined the branches characteristic, the load and generation profiles (so the net apparent power for each node), it is possible to evaluate the nodal voltages, the branches current and the power flow distribution through the application of the Backward and Forward Sweep. This algorithm can be applied in this study because the grid analysed has a radial distribution. Instead, due to its working principle, the Backward and Forward Sweep cannot solve the system of equations when applied to a meshed grid. The steps of this iterative algorithm are:

- Initialization. In this step, the counter $k=1$ is fixed and so is the initial voltage, for each node.

$$U_i^{(0)} = 1 \text{ p.u. for each node}$$

- Backward sweep. In this step the load currents are calculated with *Equation 2.4*. Then the branches current can be evaluated starting from the further loads currents and summing them backward up to initial node of the radial grid applying the Kirchhoff Current Law (*Equation 2.5*). Note that letters i and j refer to two different nodes.

$$\bar{I}_i^{(k)} = \frac{P_i - jQ_i}{U_i^{(k-1)}} \quad (2.4)$$

$$I_{ij}^{(k)} = \sum_{i=j}^{\text{downward nodes}} \bar{I}_i^{(k)} \quad (2.5)$$

- Forward sweep. Knowing the branch currents and impedances, the new nodal voltages can be calculated as in *Equation 2.6*.

$$\bar{U}_i^k = \bar{U}_j^k - \bar{Z}_{ij} \cdot \bar{I}_{ij}^k \quad (2.6)$$

- Convergence check. The iterative process stops when the difference between the voltage at previous time step and the current voltage of the same node is lower than a set threshold (*Equation 2.7*). Otherwise, the counter is increased of one step, the new voltage for the whole nodes is set to $\bar{U}_i^{(k)} = 1$ and the cycle starts again from the backward sweep step.

$$\max \left(\frac{|\bar{U}_i^{(k)} - \bar{U}_i^{(k-1)}|}{\bar{U}_i^{(k-1)}} \right) < \text{threshold} \quad (2.7)$$

The integration of algorithm described in the MATLAB environment is investigated in Appendix B. The logical scheme of the Backward and Forward Sweep algorithm is reported in *Figure 2.6*.

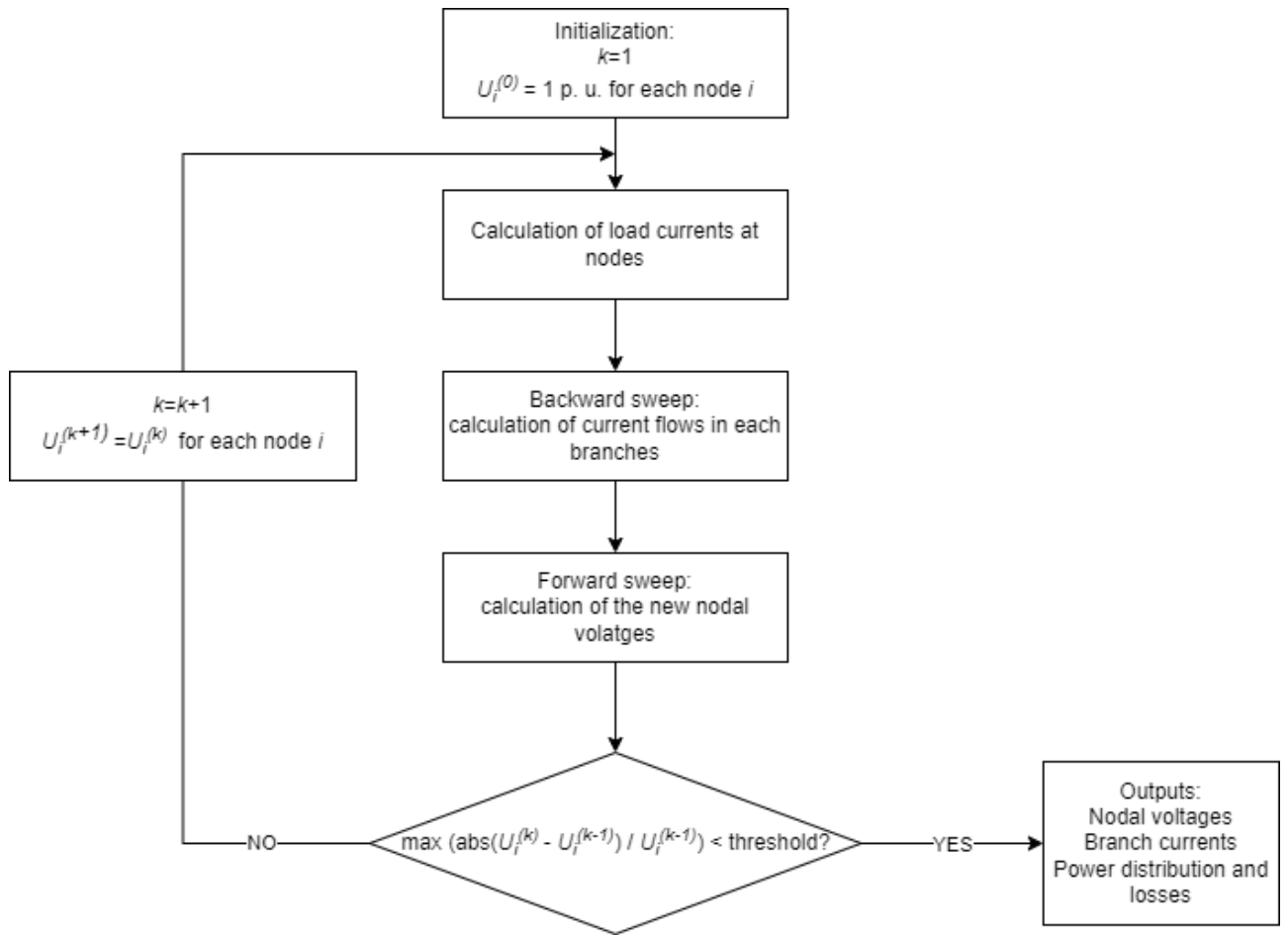


Figure 2.6 Block diagram of the Backward and Forward Sweep algorithm.

3. Modelling of the Power-to-X processes

The modelling of the three processes, that is performed in MATLAB environment, consists of the definition of the several components and their consumption and on the implementation of the working strategy.

For what concern the consumptions, they are defined depending on the process considered. The consumption difference among the three PtX can be summarised as the consequence of the different working conditions of the reactors, the possible recirculation of not-reacted reactants, the various reaction enthalpies, and different separation processes of the products.

Instead, regarding the strategy, it remains fixed for the three processes studied. Indeed, the strategy, which will be analysed in detail, is based on two parameters that are independent from the process considered: the grid surplus electric power and the hydrogen storage level.

To better understand how the three PtX plants are modelled, a simplified scheme of the model components is reported (*Figure 3.1*).

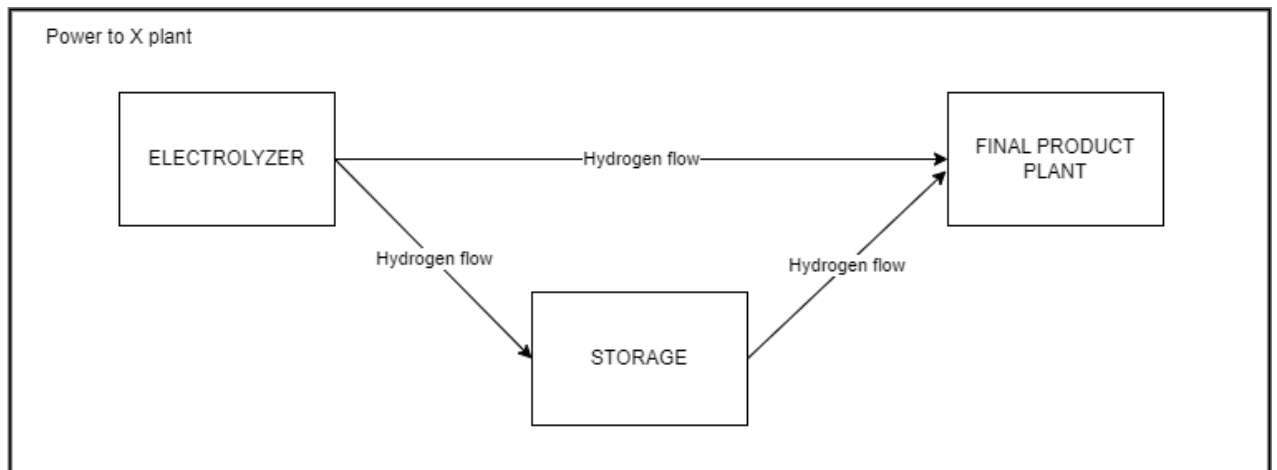


Figure 3.1 Simplified scheme of the PtX plant components

It is possible to notice that the whole PtX plant can be broken down into three macro blocks:

- Electrolysis plant.
- Hydrogen storage.
- Final product plant (FPP), that convert hydrogen and carbon dioxide in the desired product.

By changing the last block, the differentiation of the PtX studied, so of the resulted product (methane, syngas or methanol), can be obtained. Furthermore, the scheme also shows the possible hydrogen flows exchanged among the plant blocks determined by implemented strategy. The choice of modelling a Power-to-Methane, a Power-to-Syngas and a Power-to-Methanol plant relies on several interesting considerations. The first is related to the aim of differentiating the typology of process considered as much as possible. In fact, a variation of the PtX leads to distinct consumptions and model responses that allow to study if and how much this variable could affect the grid functioning and the outcomes. From this point of view, the methane synthesis requires much less energy than the methanol and the syngas ones. The second consideration springs from a possible utilisation of the final products. All the three products can be employed as raw materials in many sectors and currently they have a wide market. Moreover, thanks to their multifunctional roles, the products can be deemed as the joining point of several energetic and industrial fields. All the three processes can link the electricity network with other business, like the chemicals production and the fuel synthesis. For example, the Power-to-Methane could link the electric grid with the gas network. The methanol production could connect the electricity management to the transport sector blending it with gasoline as fuel for ICE. The syngas, instead, could be considered as a raw material for the synthesis of long chain hydrocarbons or for the ammonia production.

Another thing related to the Power-to-X models to be stressed out is the modularity of the plants. Indeed, starting from the electrolyser, the requested size is obtained considering many modules connected in parallel. Then the FPP plant size is defined on the amount of hydrogen produced by the electrolyser. In fact, the numerous element consumptions of the FPP plants and of the hydrogen compression stage are expressed as function of the hydrogen flow rate.

In the following paragraphs the different PtX plant blocks and the working strategy will be analysed individually and in depth.

3.1 Electrolyser

The most known electrolysis reaction in the energy field is that of the splitting of water molecules into hydrogen and oxygen molecules (*Equation 3.1*).



Since the Gibbs' free energy is positive (237 kJ/mol), the reaction is not spontaneous [20]. This means that for the reaction to take place an energy consumption is necessary.

The electrolysers are devices made of many electrolytic cells which allow the process by converting the electrical energy into the chemical one.

The typical structure of electrolysers is the following (*Figure 3.2*):

- Anode, the electrode where the oxidation half reaction occurs.
- Cathode, the electrode where the reduction half reaction occurs.
- Electrolyte, the separator between cathode and anode which allows only the ions transfer.

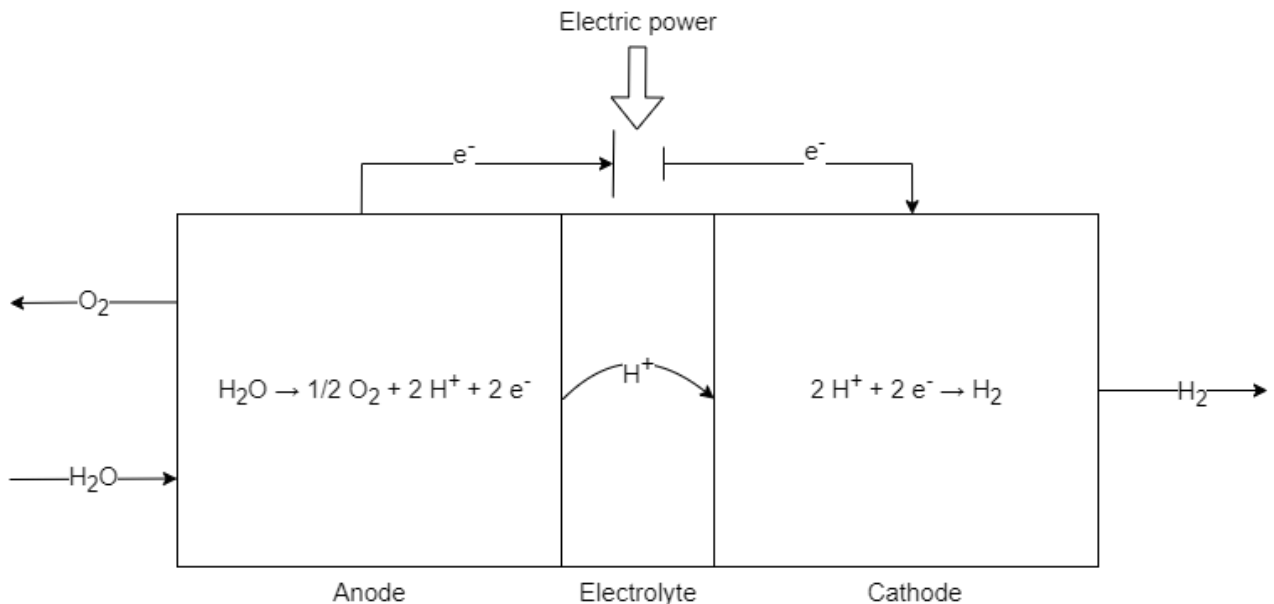


Figure 3.2 Electrolyser structure (PEMWE)

One of the distinctions among the different type of the electrolysers is the working temperature. Indeed, the electrolysers are divided into Low Temperature Electrolyser (LTE) and High Temperature Electrolyser (HTE). The LTE ones (<100°C) are subject to few

thermal stress, short warm up time, but the efficiency is the highest. The HTE ones (550-800°C) instead, have high efficiencies, but they are not suitable for frequent start and stop operations, and they suffer thermal stress more.

The main electrolysis technologies are: Alkaline Water Electrolyser (AWE), Proton Exchange Membrane Water Electrolyser (PEMWE), and Solid Oxide Water Electrolyser (SOWE). AWE and PEMWE work at low temperature, and they are reliable technologies spread on the market, while SOWE works at high temperature, and it is still under-development.

In the PtX model, the electrolysis type considered is the PEMWE for two main reasons:

- the low working temperatures allow a rapid start and stop, a quick response from the plant and a reduction in energy costs in the stand-by phase.
- it is a widely spread technology in the market.

However, there are other advantages related to these technologies, such as the plant modularity which will, therefore, allow to reach the desired sizes, by modifying the number of modules installed and the plant compactness.

The PEMWE consists of electrodes composed of a porous structure (generally, graphite) on which the catalyst (platinum group metal) is deposited, and the electrolyte represented by NAFION (Teflon polymer structure modified with a side chain ending with HSO₃).

The voltage required for the electrolytic cell to make the hydrolysis reaction take place is represented by the sum of the equilibrium voltage, the activation overvoltage, the ohmic overvoltage and the concentration overvoltage (*Equation 3.2*).

$$V_{cell} = V_{rev} + \eta_{act} + \eta_{ohm} + \eta_{conc} \quad (3.2)$$

V_{rev} represents the voltage measured at the two electrodes in the equilibrium condition, i.e. at open circuit. It can be calculated as the ratio between the Gibbs' free energy of the reaction ($\Delta_r \tilde{G}^0$, J/mol) and the product of Faraday's constant (F , 96485 C/mol) and z (charge number), a relationship known as the Nernst' law (*Equation 3.3*):

$$V_{rev} = -\frac{\Delta_r \tilde{G}^0}{z \cdot F} \quad (3.3)$$

Where the Gibbs' free energy of the reaction is expressed by means of *Equation 3.4*. In this equation, ν_i represents the stoichiometric coefficient of a generic i-th species, $\Delta_f \tilde{G}_i^0$ (J/mol) represents the Gibbs' free energy of formation of a generic i-th species, N_p is the number of products of the reaction and N_r is the number of reactants.

$$\Delta_r \tilde{G}^0 = \sum_{i=1}^{N_p} (\nu_i \cdot \Delta_f \tilde{G}_i^0) - \sum_{j=1}^{N_r} (\nu_j \cdot \Delta_f \tilde{G}_j^0) \quad (3.4)$$

For the hydrolysis reaction, assuming the reaction temperature and pressure, respectively, equal to 333.15 K (60°C) and 40 bar, V_{rev} equals to 1.19V.

η_{act} is the activation overvoltage, i.e. the additional voltage necessary to allow the start of the two half-reactions at the anode and at the cathode. Analytically, this term can be expressed as in *Equation 3.5*.

$$\eta_{act} = \frac{R \cdot T_{cell}}{n_{RDS} \cdot \beta \cdot F} \operatorname{senh}^{-1} \left(\frac{i}{i_o} \right) \quad (3.5)$$

R is the universal gas constant (8.314 J/mol · K), T_{cell} is the cell temperature equal to 333.15K, n_{RDS} is the number of electrons exchanged at rate deterministic step, β is symmetry factor, a dimensionless value, and i_o is the exchange current density (A/cm²).

η_{ohm} is the ohmic overvoltage, which takes into account the voltage drop linked to the resistances that the electrolyte and the electrode linking cable oppose to the transfer of charge (in the case of PEMWE electrons e⁻ and H⁺ ions). This term can be expressed by referring to Ohm's law (*Equation 3.6*).

$$\eta_{ohm} = ASR \cdot i \quad (3.6)$$

Where

$$ASR = \rho \cdot L \quad (3.7)$$

ASR is the Area Specif Resistance of the cell ($\Omega \cdot \text{cm}^2$), ρ is the electric resistivity of the conducting material ($\Omega \cdot \text{cm}$), and L is the length of the pathway that the charged species has to cover (cm).

η_{conc} represents the overvoltage linked to the phenomenon of the reactants diffusion. In fact, in order to be able to react, the reactants must penetrate the porous matrix of the

electrodes, until they reach the conversion zone. The concentration overvoltage takes into account the resistance opposed by the electrodes to the diffusion of the reactants. The more PEMWE works at high flow rates, the greater the speed with which the reagents are consumed compared to the speed with which they spread, and the greater the weight of this type of inefficiency on the process [21]. It can be evaluated as follows (*Equation 3.8*).

$$\eta_{conc} = \frac{R \cdot T_{cell}}{z \cdot F} \cdot \ln\left(1 - \frac{i}{i_l}\right) \quad (3.8)$$

i_l is the limiting current density (A/cm^2), which represents the maximum current that can be elaborated by the electrode.

In the study under examination, in order to model the electrolytic cell, reference is made to characteristic parameters of experimental nature [22]. In the model considered, the three overvoltage are evaluated as in *Equations 3.9 - 3.10 - 3.11*.

$$\eta_{act} = a + b \cdot \ln(i) \quad (3.9)$$

$$\eta_{ohm} = R_{ohm} \cdot i \quad (3.10)$$

$$\eta_{conc} = m \cdot e^{(n \cdot i)} \quad (3.11)$$

Where parameters a , b , R_{ohm} and m are calculated starting from empirically defined values, shown in the *Table 3.1* [22].

$$a = a_0 + a_1 \cdot T_{cell} \quad (3.12)$$

$$b = b_0 + b_1 \cdot T_{cell} \quad (3.13)$$

$$R_{ohm} = R_{ohm,0} + R_{ohm,1} \cdot T_{cell} \quad (3.14)$$

$$m = m_0 + m_1 \cdot T_{cell} \quad (3.15)$$

Table 3.1 PEMWE polarization curve parameters [22]

Type of overpotential	Parameters	Value
Activation	a_0 (V)	0.6259
	a_1 (V/K)	$-1.1128 \cdot 10^{-3}$
	b_0 (V)	$9.1487 \cdot 10^{-2}$
	b_1 (V/K)	$-1.4866 \cdot 10^{-4}$
Ohmic	$R_{ohm,0}$ (Ω)	$2.8959 \cdot 10^{-3}$
	$R_{ohm,1}$ (Ω /K)	$-4.8479 \cdot 10^{-6}$
Concentration	m_0 (V)	$1.8250 \cdot 10^{-2}$
	m_1 (V/K)	$-3.3280 \cdot 10^{-5}$
	n (A^{-1})	$4.500 \cdot 10^{-2}$

Having defined the parameters characterizing the cell, it is then possible to express the cell voltage as a function of the processed current. By providing the model, implemented in the MATLAB environment, with the vector of the currents processed by the cell, it is possible to construct the characteristic polarization curve (Figure 3.3).

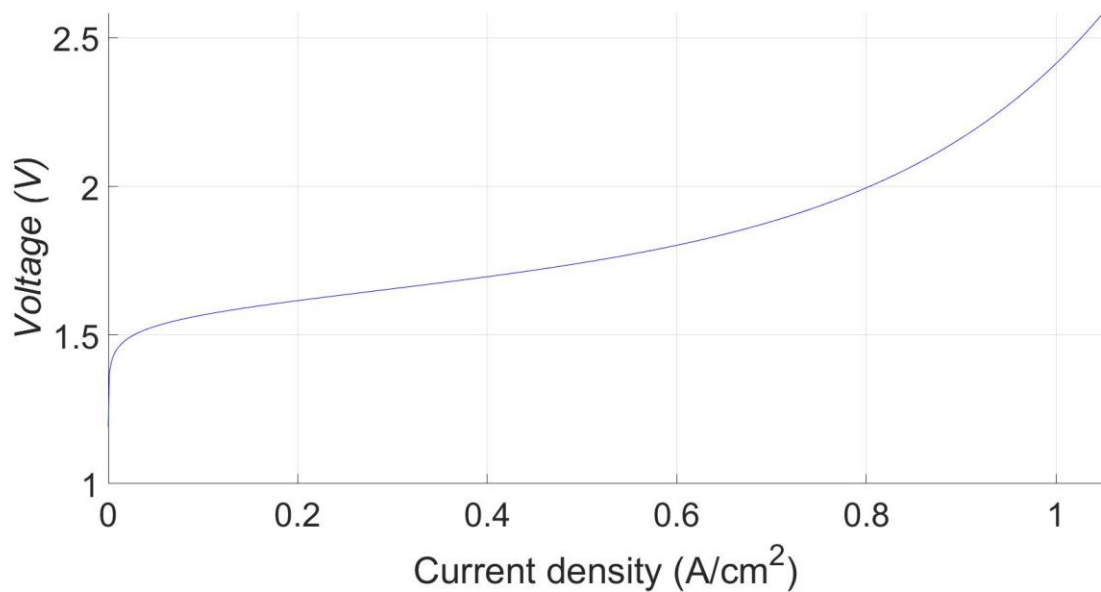


Figure 3.3 PEMWE cell polarization curve.

To switch from a single electrolytic cell to the electrolyser model, two assumptions are made: the area of a single cell is 100 cm² and the stack consists of 1300 cells arranged electrically in series but provided with reactants in parallel [22].

In this way, the electrolyser has a nominal power of 200 kW. As a result of the modularity, it is possible to install several modules in parallel to reach the desired sizes.

Additionally, thanks to Faraday's law (*Equation 3.16*), the moles per second of hydrogen produced by varying current processed by PEMWE can be calculated:

$$n_{H_2} = \frac{n_{cell} \cdot A_{cell} \cdot i}{z \cdot F} \quad (3.16)$$

Figure 3.4 shows the flow rate of hydrogen produced as a function of the power absorbed by the electrolyser.

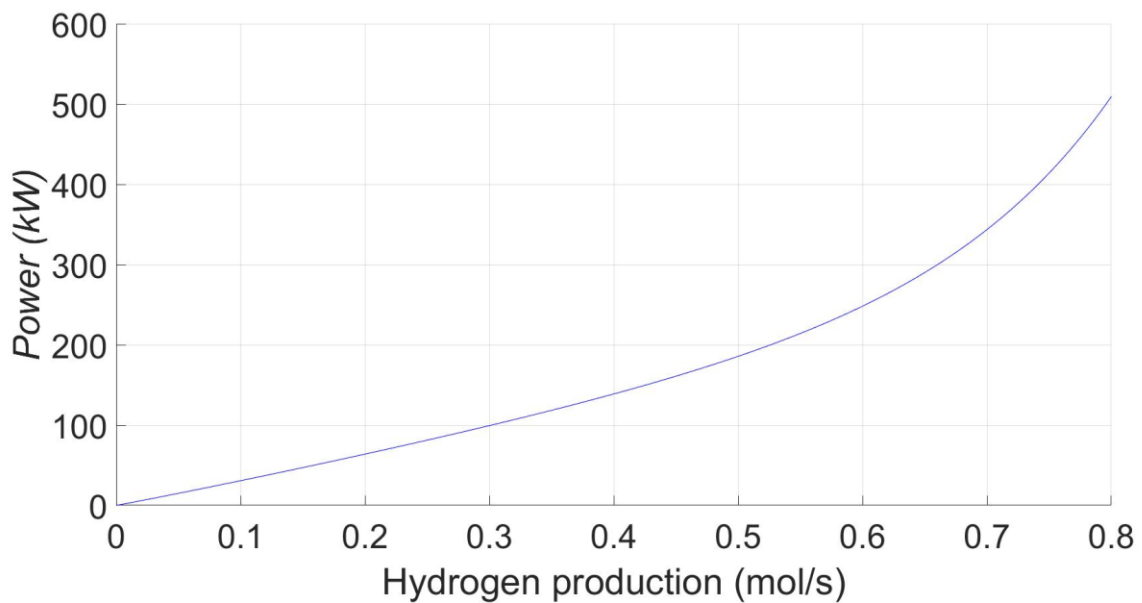


Figure 3.4 PEMWE hydrogen production as function of power absorbed.

It is noteworthy that for high hydrogen flow rates there is a significant increase in the power absorbed by the electrolyser. This is due to the increase of transport phenomenon, especially the concentration one, therefore bringing to the rapid decrease of the efficiency of the process (*Figure 3.5*).

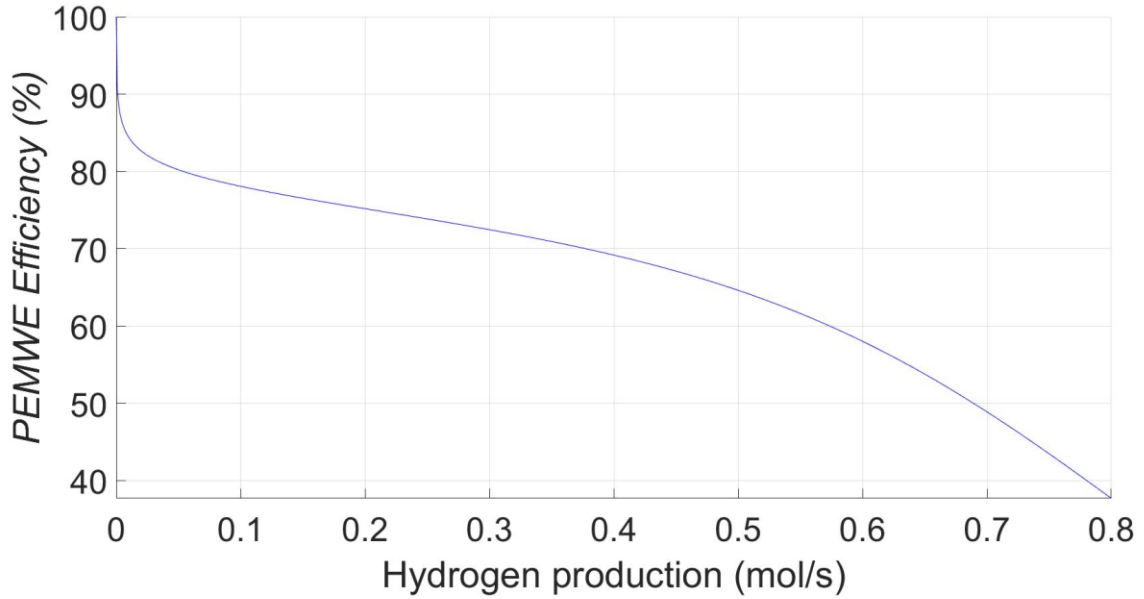


Figure 3.5 PEMWE Efficiency

The efficiency of the electrolyser (Equation 3.17) is calculated as the ratio of the chemical energy, represented by the product between the flow of hydrogen produced and the LHV of the hydrogen (120 MJ/kg [23]), and the electrical energy absorbed:

$$EFF = \frac{n_{H_2} \cdot PM_{H_2} \cdot LHV_{H_2}}{P_{el}} \quad (3.17)$$

The PEMWE model, including the auxiliary, is shown in Figure 3.6.

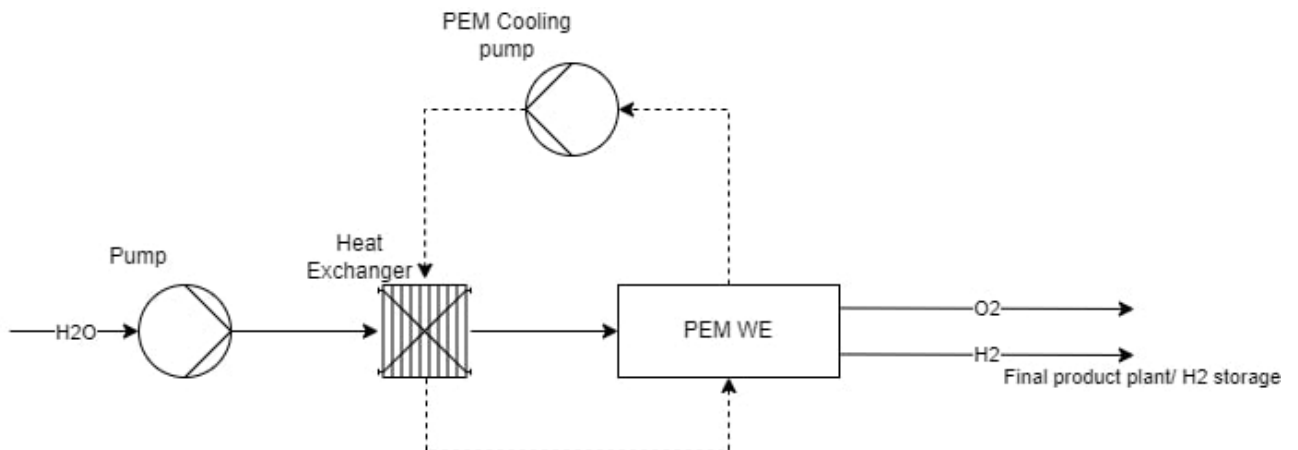


Figure 3.6 Electrolyser plant scheme

The working conditions of the PEMWE are assumed to be at a temperature of 333.15 K (60°C) and a pressure of 40 bar. Work at high pressure is a benefit since the gas compression is more expensive from the power consumption point of view than the water compression. The other electrical consumptions, apart from the PEMWE, are represented by the pumps

for the inlet water compression and for the cooling loop. They are estimated as in *Equation 3.18*.

$$W_{pump} = \frac{k \cdot Q \cdot g \cdot \Delta P}{\eta_{pump}} \quad (3.18)$$

The efficiency of the pump is set at 0.85 [24]. Q represents the water flow rate elaborated by the pump. k is a conversion factor and ΔP represents the pressure jump impressed by the pump.

The electrolyser model described is common to the three different PtX plants since the hydrogen is used later as reactant both for the production of methane, and syngas and methanol.

3.2 Methanation

Methane is the shortest hydrocarbon; it is made of one carbon atom linked with single bounds to four hydrogen atoms. At standard conditions, it is a colourless and odourless gas, and it is inflammable, but not toxic. Methane is abundant on earth and can be found mainly in impermeable storages under the soil as natural gas (fossil source). It can be obtained also as product of anaerobic digestion of organic matters known as biogas (biological source) or by the gasification of the coal or of the biomass. The natural gas usually can have a high concentration of methane (up to 90% in volume basis) while the biogas usually has lower concentrations [25]. Among the several greenhouse gases, the methane is the worst hydrocarbon from the environmental point of view, since its global warming potential on one hundred years reference is 28 times higher than the one of the carbon dioxide [26].

The methane is largely used in several sectors, varying from the energy production to the transport domain and to the chemical factories. In 2019, the natural gas (mainly composed by methane) represented 23.2% of the world total energy supply, equivalent to 140.8 EJ [27]. In 2020, the major producers of natural gas are the OECD countries (Organisation for Economic Co-operation and Development) with 38.4%, followed by the non-OECD Europe and Euroasia with 23.8% and then by the Middle East countries with 16.1% [27]. Apart from the energetic uses, methane is employed for the ammonia synthesis for fertilisers and

explosives production. The incomplete combustion elements are used to produce vehicle tires [25].

Methanation is a chemical-physical process that allows to obtain methane and water starting from hydrogen and carbon dioxide. The main reaction that occurs is (*Equation 3.19*):



The reaction is strongly exothermic, since $\Delta_r \tilde{H}_{298.15K}^0 = -165.1$ kJ/mol, and is therefore favored at low temperatures and high pressures. Consequently, the operating conditions at which the reaction takes place are at a temperature of 250°C and a pressure of 15 bar. The methanation is usually made up of several catalytic reactors arranged in series (multi-stage process) in order to optimize the conversion to methane, better control the temperature of the reactors, and ensure that the output product has the desired specifications. Generally, the applied catalysts fall within the VIII-X metal group and are arranged on a support layer represented by metal oxides (Al₂O₃) [28], [29].

To have a complete view of the entire methanation process with auxiliary annexes it is possible to refer to the *Figure 3.7*.

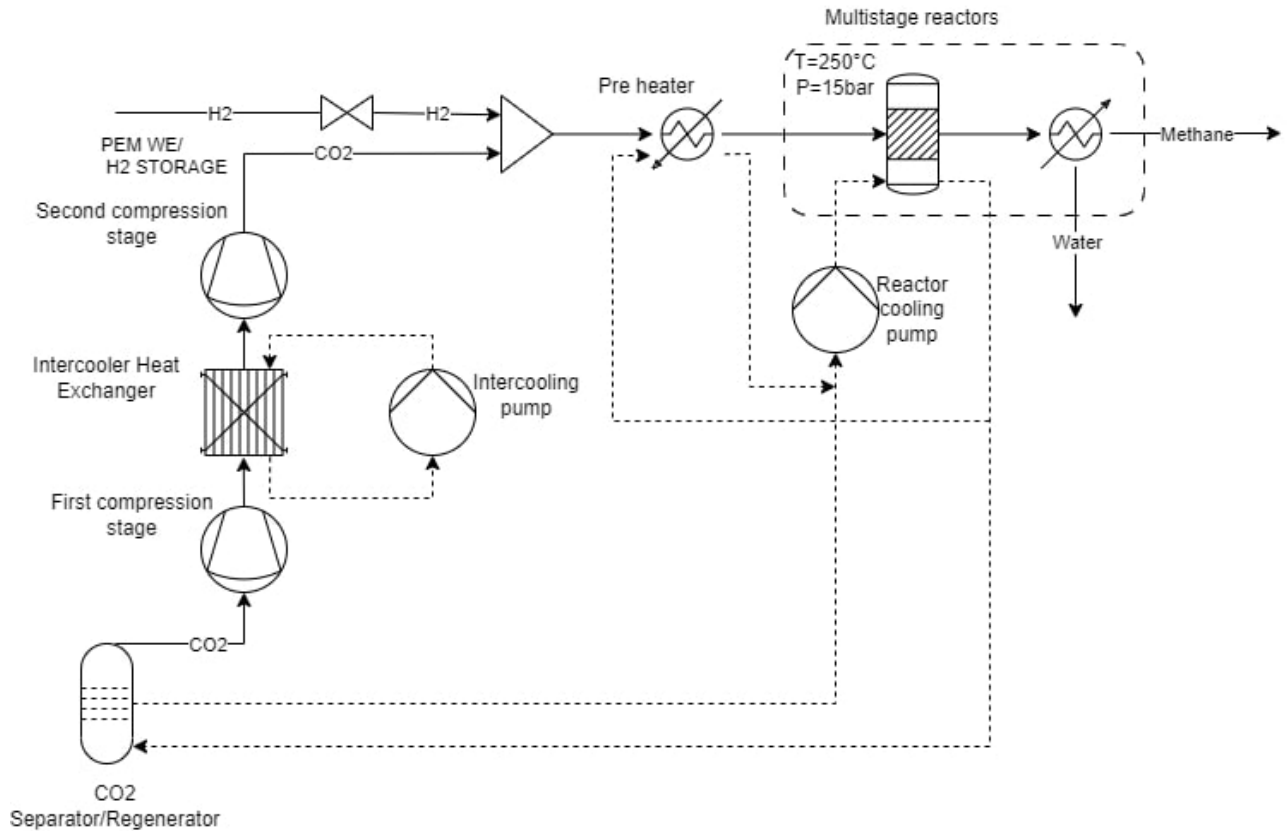


Figure 3.7 Methanation plant scheme

The model also considers the consumption related to the separation of CO₂ that will then be used as a reagent together with hydrogen in the methanation reactor. Nowadays there are different Carbon Capture (CC) technologies. These differ according to the source of CO₂ treated (flue gases, ambient air, biogas plant) and the kind of process implemented. The most common CC technologies are: chemical absorption, separation membrane, adsorption-based (Pressure Swing Adsorption and Temperature Swing Adsorption) and cryogenic separation. The study suggested the application of a separation process to chemical absorption with Monoethanolamine (MEA) (more information is reported in Appendix A). The energy costs linked to the CO₂ separation, equal to 3 MJ/kgCO₂, are mainly related to solvent regeneration [30]. The separated CO₂ is compressed, through centrifugal compressors that process high flow rates at low compression ratios, up to the working pressure of the methanation reactors. Since $\frac{P_{fin}}{P_{in}}$ is elevated, it has been considered a two-stage compression ($N_c=2$) with intercooling, so as to keep β_c below 4. Specifically, β_c has been evaluated as in Equation 3.20.

$$\beta_c = \sqrt[n_c]{\frac{P_{fin}}{P_{in}}} \quad (3.20)$$

While the power needed/required for compression is defined in *Equation 3.21*.

$$W_c = \frac{Z * R * T_{in} * \gamma * \eta_c}{\gamma - 1} * \left(\beta_c^{\left(\frac{\gamma-1}{\gamma * \eta_c}\right)} - 1 \right) * n_{CO_2} \quad (3.21)$$

Where the CO₂ heat capacity ratio, γ , at inlet temperatures and pressures are set at 1.241 for the first stage and 1.255 for the second stage [31]. Z , the compressibility factors are also tabulated values in the literature [32]. The compressors efficiency is set to 0.85 [24]. T_{in} is the temperature of the stream at the inlet of the compressor (K) and n_{CO_2} is the CO₂ molar flow rate (mol/s).

Between the two compressors there is a heat exchanger that allows to cool the compressed CO₂, heat to the refrigerant circulated by a pump. The power required by the pump is calculated with the equation 3.18.

The compressed CO₂ is mixed with the depressurized hydrogen of PEMWE/storage. The lowering of hydrogen pressure leads to a slight heating of the gas (*Equation 3.23*), being its Joule-Thomson coefficient negative and evaluated as (*Equation 3.22*):

$$\mu_{JT} = \frac{\frac{2 \cdot a}{R \cdot T} - b}{C_p} \quad (3.22)$$

$$\Delta T_{JT} = \Delta P \cdot \mu_{JT} \quad (3.23)$$

a and b are the van der Waals coefficients for the H₂ [33], μ_{JT} is the Joule-Thomson coefficient (K/bar), C_p is the specific heat capacity at constant pressure (J/mol·K), and ΔP represents the pressure reduction (bar).

Then the reactant mixture is preheated in order to reach the methanation temperature.

Part of the heat required for preheating and all the heat required for MEA regeneration in the CO₂ separation phase is supplied by cooling the methanation reactors. As a matter of

fact, it is good to remember that the formation reaction of methane leads to the release of high thermal energy, being the exothermic reaction. In particular, the enthalpy of reaction at the process temperature is evaluated by first calculating the enthalpy, entropy and Gibbs' free energy of the individual components of the reaction (Equations 3.24 – 3.25):

$$H^\circ(T) = A \cdot t + B \cdot \frac{t^2}{2} + C \cdot \frac{t^3}{3} + D \cdot \frac{t^4}{4} - \frac{E}{t} + F \quad (3.24)$$

$$S^\circ(T) = A \cdot \ln(t) + B \cdot t + C \cdot \frac{t^2}{2} + D \cdot \frac{t^3}{3} - \frac{E}{2 \cdot t^2} + G \quad (3.25)$$

A, B, C, D, E, F, G factors are tabulated values [34], t is the temperature (K/1000).

Subsequently, the reaction enthalpy is determined by applying Hess's Law (Equation 3.26):

$$\Delta_r \tilde{H}^0 = \sum_{i=1}^{N_p} (v_i \cdot \Delta_f \tilde{H}_i^0) - \sum_{j=1}^{N_r} (v_j \cdot \Delta_f \tilde{H}_j^0) \quad (3.26)$$

Referring to the reaction temperature of 250°C, $\Delta_r \tilde{H} (T_{react}) = -175.81$ kJ/mol.

At the outlet section of the reactors the water is separated from the synthetic natural gas by a quickly cooling of the mixture flow rate. To be able to condensate the water at a pressure of 15 bar, its temperature should be decreased below 198°C. To ensure this to happen, it is considered a water-cooling loop coupled with an industrial forced convection evaporative cooling system [35].

To sum up, the consumptions of the product separator unit are the power needed by water recirculation pump (evaluated with equation 3.18), and the power absorbed by the forced convection cooler. This last consumption is assumed fixed, so it does not vary with the flow rate to cool down.

It can be emphasised that the total consumption of this FPP is the lowest among the Power-to-X technologies. This is mainly due to the exothermicity of the methanation reaction that reduces the electric heater consumption for the MEA regeneration and the preheating of the reactants. The major consumption is related to the power absorbed by the CO₂ compression stages.

3.3 Methanol synthesis

Methanol is the smallest and simplest alcohol made of an atom of carbon with three bonds with hydrogen atoms and one with a OH group. At standard ambient conditions it is a transparent liquid, highly inflammable. Methanol is largely used as a raw material for the production of many chemicals as solvents, drugs, additives, and resins. Going more into detail, the plastic production factories are the largest consumers of methanol. They use this raw material to produce the base elements (formaldehyde, terylene) of many plastics (Plexiglas, polyethylene, polypropylene). The second main consumption is as fuel at its unaltered status. Recently, the methanol consumption as fuel is increasing more and more. For example, in China, methanol can be burned in the currently IC engines blended with the gasoline up to 15% without modifying the engine. However, by changing it, the engine can work with the fuel composed up to 85% of methanol [36]. In addition, not only in the road transport sector, but also in the marine one, the methanol could represent a valid alternative to the fossil fuel consumption, as suggested by the Stena Line project. The third highest demand of methanol is represented by the fuel production factories. The methanol, indeed, can be converted in gasoline passing through the dimethyl ether synthesis. Other methanol demands are linked to the gasoline additive productions as t-amyl methyl ether. Currently, the global yearly methanol production is estimated to be equal to 110 billion of tonnes, representing a fast-growing market [37], [38].

The methanol synthesis is a process based on the CO₂ hydrogenation too, where the final product is obtained as the equilibrium of two main reactions (*Equations 3.27 – 3.28*):



The former reaction is the reverse water gas shift, its enthalpy is positive, while the latter is largely exothermic. Synthetising, the global reaction can be expressed as in the *Equation 3.29*.



$\Delta_r \tilde{H}(T_{react}) = -57.2$ kJ/mol is calculated as in the methanation case, determining firstly the elements enthalpy and entropy at reaction temperature, and then applying the Hess law. Due to the exothermicity of the reaction, the temperature of reaction is fixed to 250°C while the pressure is set to 50 bar to enhance the methanol production. The methanol synthesis reactor usually is made by several pipes where the catalysts (Cu/Zn/Al/Zr) are deposited on the surface to improve the reactants conversion.

The following model considered is reported and already studied in literature [39]. A global scheme of the methanol synthesis plant is represented in *Figure 3.8*.

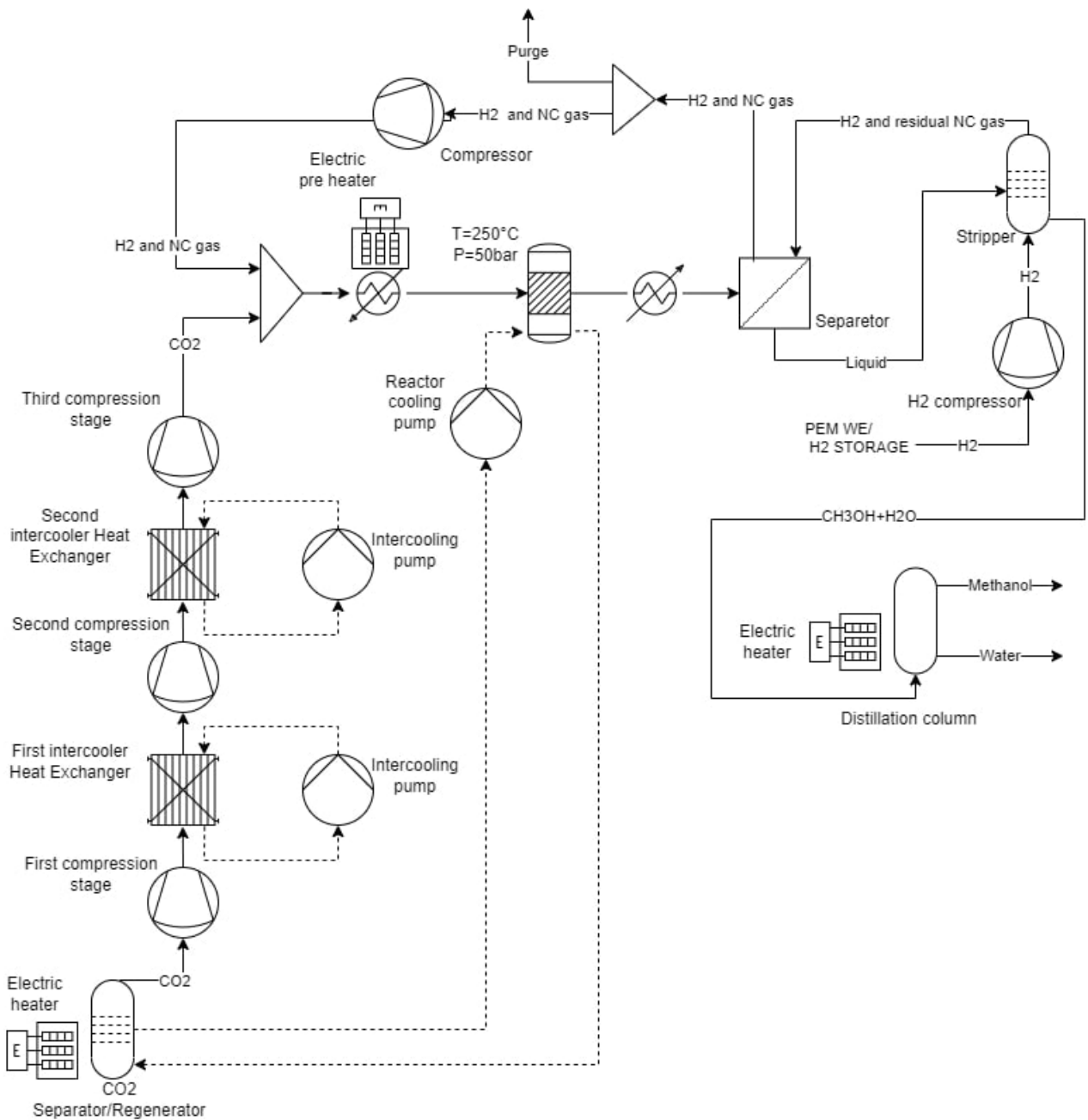


Figure 3.8 Methanol synthesis plant scheme

The CO₂ stream is obtained from the CC based on the MEA absorption technology. In this scenario the heat needed for the regeneration of the MEA is furnished partially from the heat released by methanol synthesis reaction and partially from an electric heater. The CO₂ separated is compressed at 50 bar through three compression stages with intercooling steps. Then it is mixed with H₂ and non-condensable gas and heated up with electric heater before to be sent to the reactor. At the outlet section the products are cooled down and then the liquid part is separated from the gaseous one. The latter one is partially recirculated back to the inlet of the reactor and partially (1.5% of the total flow) is purged. The liquid part is

sent to a stripper where interacts with compressed hydrogen in counter-current mode. Hydrogen removes the non-condensable gases (CO and CO₂) from the fluid (mostly methanol and water). The hydrogen and the others non-condensable gases are recirculated back to the separator, while the liquid is sent to a distillation column for the water/methanol separation. The heat needed to separate the product is supplied by an electric heater.

The compression and the pumping power needed and the amount of heat to be removed or to be supplied to the process are estimated referring to the model studied by Kiss et al, [39]. The model consumption is estimated scaling the consumption reported in literature as the ratio between the flow rates considered.

For the methanol production, the consumption assumes intermediate values among the other two plants studied, because the enthalpy of reaction partially covers the heat demand of the plant. The consumptions are mostly due to the MEA regeneration, the CO₂ compression since it has to reach high pressure, and to the product separation.

3.4 Syngas synthesis

The syngas, the abbreviation of synthetic gas, is mainly a mixture of hydrogen and carbon monoxide. It can be found at different H₂/CO ratios, usually starting from a minimum value of 0.5 and up to 4. It is a very ductile gas. At ratios close to 2, it can be used as a raw material in Fischer-Tropsch process for the production of many chemicals and of medium-long chain of synthetic fuel [40], [41]. It can be also blended into natural gas to be burned in gas turbine for energy production. By the way, the current syngas market is focused on the ammonia production, followed by hydrogen and methanol refineries, then by the gas-to-liquid industries and, finally, by the electricity production. Globally, each year, the syngas synthesis is estimated to be equal to 6 EJ, representing the 2% of the world primary energy consumption [42].

The reaction considered in our model for the synthesis of syngas is the reverse water gas shift (*Equation 3.30*):



Applying the Hess law, the $\Delta_r \tilde{H} (T_{react})$ is evaluated as 34.1 kJ/mol. The endothermicity of the reaction suggest operating at high temperature for its thermodynamic equilibrium, while it does not depend on the working pressure. The following assumptions are done: the reaction temperature is set to 800°C, the pressure to 5 bar and an outlet ratio R between H₂ and CO equal to 2. The RWGS reaction is enhanced by the application of a catalyst layer, usually represented by a noble metal as Pt, Ru and Au [43].

The syngas ratio, together with the operating conditions, affects the selectivity of the products of the Fischer-Tropsch process and also the catalyst to use. In *Figure 3.9* the scheme of the process is reported.

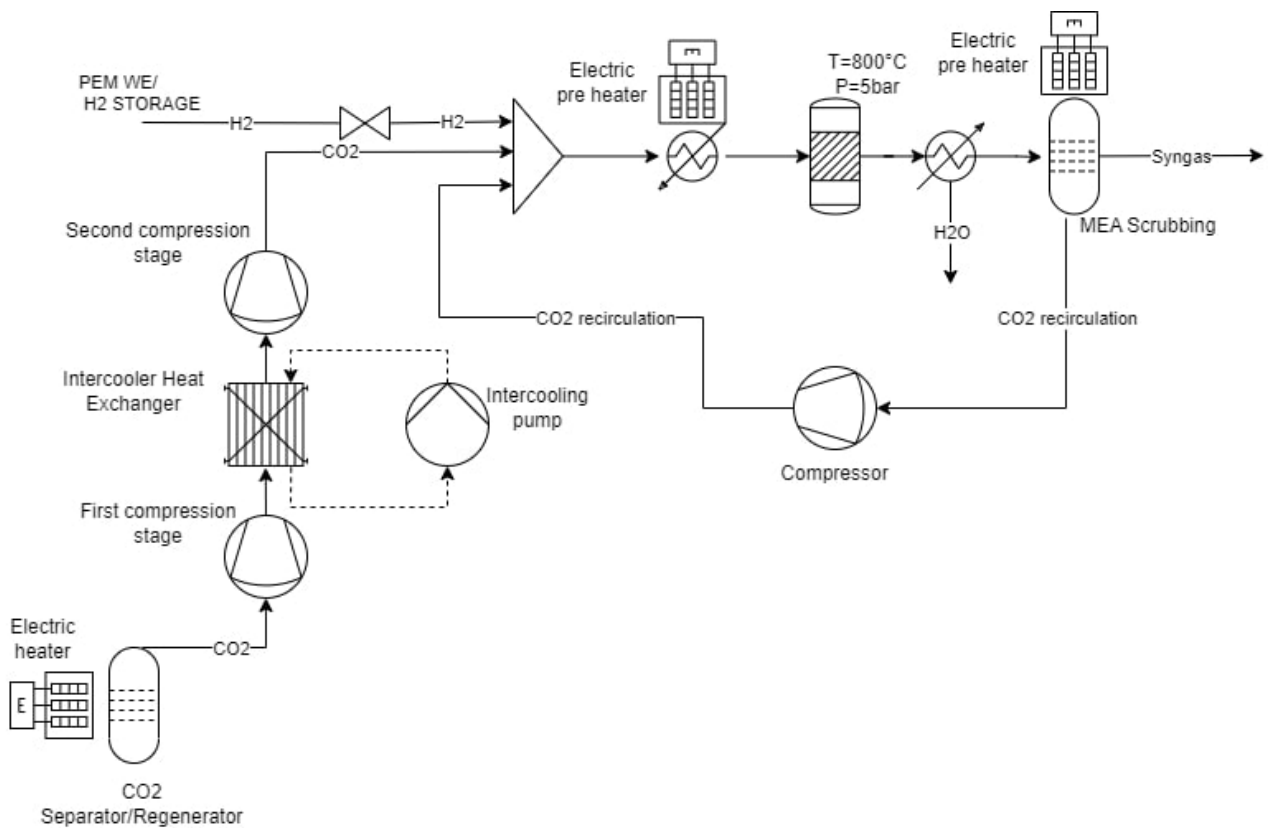


Figure 3.9 Syngas plant scheme

The carbon dioxide, representing a reactant of the RWGS, is obtained through the regeneration of the MEA. The heat necessary to release the CO₂ is fully supplied by an electric heater since, unlike the other two processes analysed, the heat does not come from the cooling of the reactor. A two steps compression is needed to reach the process pressure. Hydrogen is depressurised and heated proportionally to the JT coefficient as expressed in the *Equation 3.23*.

To find the inlet and outlet mixture composition and, the amount of recirculated CO₂ (to achieve the set H₂/CO ratio), firstly the K_{eq} is calculated applying *Equation 3.31*:

$$K_{eq} = e^{\left(-\frac{\Delta G_{react}}{R \cdot T_{react}}\right)} \quad (3.31)$$

Then is possible to solve the following system of equations where Y represents the molar fractions of the species and χ the grade of advancement of the reaction (*Equations 3.32*):

$$\begin{cases} Y_{H_2out} = Y_{H_2in} - Y_{CO_2in} \cdot \chi \\ Y_{CO_2out} = Y_{CO_2in} \cdot (1 - \chi) \\ Y_{H_2Oout} = Y_{H_2Oin} + Y_{CO_2in} \cdot \chi \\ Y_{COout} = Y_{COin} + Y_{CO_2in} \cdot \chi \\ K_{eq} = \frac{Y_{H_2Oout} \cdot Y_{COout}}{Y_{H_2out} \cdot Y_{CO_2out}} \end{cases} \quad (3.32)$$

Fixing as constraints Y_{H_2Oin} and Y_{COin} equal to zero and $\frac{Y_{H_2,out}}{Y_{CO,out}}$ equal to 2, the resulting second order equation (*Equation 3.33*) to obtain the plausible value of χ ($0 \leq \chi \leq 1$) is solved.

$$\begin{aligned} (1 - K_{eq}) \cdot Y_{CO_2in}^2 \cdot \chi^2 + [Y_{COin} + Y_{H_2Oin} + K_{eq} \cdot (Y_{CO_2in} + Y_{H_2in})] \cdot \\ Y_{CO_2in} \cdot \chi + Y_{COin} \cdot Y_{H_2Oin} - K_{eq} \cdot Y_{CO_2in} \cdot Y_{H_2in} = 0 \end{aligned} \quad (3.33)$$

Then substituting χ in each equation of the system, the mixture composition at inlet and outlet of the reactor is assessed.

The reactor inlet stream is preheated with an electric heater. At the outlet of the reactor the stream is cooled down and the condensed water is separated. Then a second CC system provides the separation of carbon dioxide from the syngas. The power consumption, represented by electricity from the grid, is related to the regeneration of MEA. At the outlet of the absorption module the purified syngas is obtained, while the CO₂ absorbed is mixed back with fresh CO₂ and H₂.

The compression and pumping power needed are estimated referring respectively to equations 3.21 and 3.18.

As seen, the syngas plant is the only Power-to-X studied that develops an endothermic reaction. That condition affects a lot the final FPP consumption, showing the highest

energetic expenditure among the plants modelled. The major consumptions are related to the heat required by the reaction to happen, to the preheating of the reactants, to the heat for the MEA regeneration, and to the syngas separation.

3.5 Hydrogen storage

The third component considered for the modelling of a PtX plant is the hydrogen storage. This has a crucial role in the model because allows to mismatch the functioning of the final product plant from the electrolyser. Indeed, on one hand, the PEMWE has a fast dynamic and can follow promptly the power surplus profile, so the amount of hydrogen produced can vary rapidly in a wide range. On the other hand, the final product plant has a slower response than the PEMWE, so the installation of a storage to work with somewhat smooth hydrogen flow rate is suggested. Furthermore, if in full conditions, the hydrogen storage allows to continue to work the FPP both when the power surplus is not able to supply the PEMWE, and when the RES does not generate any power. In this last case the FPP is an additional load for the electric grid. The element of the model considered is shown in the *Figure 3.10*.

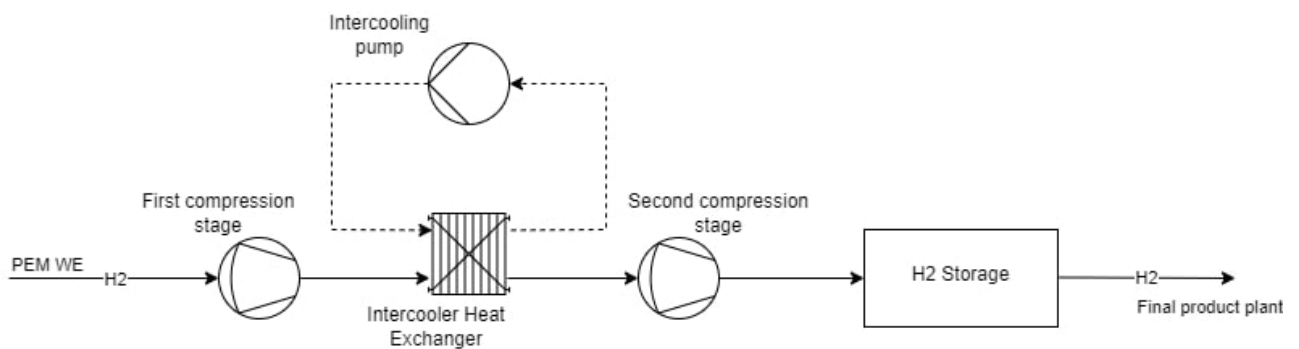


Figure 3.10 Hydrogen storage scheme

The hydrogen coming from the electrolyser is compressed up to pressure storage level of 200 bar through a two compression stages with intercooling. The consumption of the compressor and of the cooling pump are evaluated with equations 3.21 and 3.18.

An important task done in the modelling of the H₂ storage is the determination of its size. The size of the storage is evaluated considering the concept of autonomy, so the hydrogen storage capacity shall ensure a certain number of working hours (at a determined capacity factor) of the FPP in absence of hydrogen production. By that definition is possible to

determine the moles of hydrogen to be stored for achieving a certain autonomy as the *Equation 3.34*:

$$n_{H2_storage} = n_{H2_min} \cdot t_{aut} \quad (3.34)$$

Where n_{H2_min} represents the mole flow rate of hydrogen drawn from the storage (mol/s), in this model it is equal to the minimum flow rate at which the FPP can work, and t_{aut} is the autonomy (s). Evaluated the amount of mole of hydrogen to be stored, the size of the storage is defined in *Equation 3.35*.

$$V_{storage} = \frac{n_{H2_storage} \cdot R \cdot T}{P_{storage}} \quad (3.35)$$

As mentioned above, the autonomy affects the size of the storage. In literature the opinion that the choice of the storage size is a trade-off between the autonomy and the capital cost is commonly agreed. In fact, a big storage tank guarantees a longer autonomy but is economically expensive while, a small one has the opposite effect [28]. To find the best option, three level of storage autonomy are simulated: 8, 12, and 16 hours. The decision variable is the amount of time that the FPP switched on. The simulations are performed with the power to methane model in the summer reference period. The results, normalized respect to the worst case (autonomy of 8 h), show that the start and stop conditions for the autonomy of 12 h occur 31.8% less, and for the autonomy of 16 h occur 36.4% less (*Figure 3.11*).

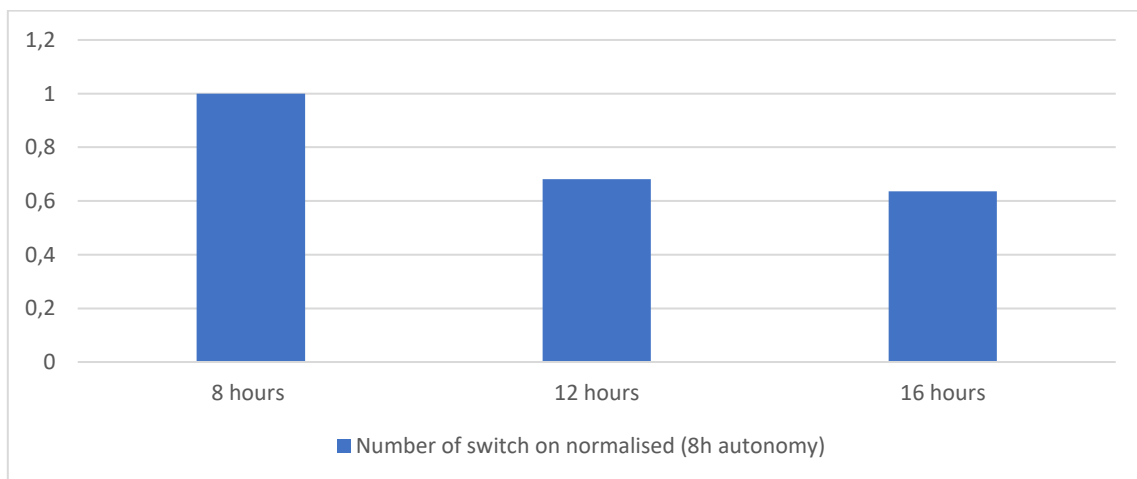


Figure 3.11 Normalised number of switch on/off of the FPP for different autonomies

As expected, the 8 h autonomy shows the highest on/off of FPP occurrence. That is due to the shutdown of the plant every night, since the amount of hydrogen stored is completely

discharged before the PEMWE starts producing and refilling the storage. Despite it has not the lowest on/off occurrence, the autonomy of the H₂ storage chosen in the modelling of the plant is 12 h since has the best compromise between cost and number of on/off occurrence.

Having defined the hydrogen storage sizes, the storage level has to be updated at each time step. The followed procedure is based on a matter balance between the moles of hydrogen already stored, the ones produced by the PEMWE sent to the compression stages, and the ones consumed by FPP. When the molar flow of hydrogen coming from the PEMWE to the storage is higher than the one that is drawn by the FPP from the storage, the hydrogen stored increases. The opposite occurs when the molar flow from the storage is higher than the one to the storage. The percentage of the storage level is calculated as the ratio between the amount of hydrogen mole stored and total amount that could be stored.

3.6 PtX model strategy

The strategy implemented in each PtX model affects deeply the results and the possible benefits that those installation could bring to the grid. It is important to highlight that the strategy is common to the three PtX plants, and the difference in the results must be attributed to the differences in the processes.

The main logic of the strategy is to try guaranteeing two conditions that are reported in order of prominence:

- the working conditions of the FPP at almost minimum load capacity to limit the switch on/off conditions.
- the filling of the hydrogen storage in order to be able to work with the FPP also when the electrolyzers cannot produce hydrogen.

The management of the electrolyser, of the storage and of the FPP takes into consideration several parameters furnished as inputs of the PtX model:

- the power surplus from the grid. It is evaluated for each time step as the difference between the generation profiles and the load profiles at each node.
- the storage level of hydrogen. The value of the previous time step is considered.

- the status of the FPP. It can assume two values, ‘1’ when switched on and ‘0’ when switched off. Also in this case, it represents the value of the previous time step.

In details the possible working conditions of the PtX components are:

- PEMWE: the electrolyser can work from a minimum load up to the nominal condition. If the power surplus from the grid is lower than the minimum working threshold, the PEMWE is set in stand-by conditions. In the case when $P_{PEMWE_{min}} < P_{surplus} < P_{PEMWE_{nom}}$, the working condition of the PEMWE is determined in order to match the power available from the grid and the power absorbed by the global plant (generation=load). The *Equation 3.36* has to be satisfied.

$$P_{surplus} = P_{PEMWE} + P_{aux} + P_{storage} + P_{FPP} \quad (3.36)$$

When the hydrogen storage is already full, the equation is still to be satisfied but the term $P_{storage}$ is set to zero. Instead, when the storage level is lower than a minimum threshold, P_{FPP} is null in the equation.

Of course, when the PtX reaches nominal condition and $P_{surplus}$ increases, the equation is not anymore satisfied.

- Storage: the management of the hydrogen storage has a key role in the global strategy and, as seen in paragraph 2.5 considers the concept of autonomy. The definition of specific storage threshold, together with the grid power surplus, are, indeed, the trigger points that determine the PtX working conditions. When the hydrogen storage is almost empty (level of the storage < minimum level threshold), the FPP plant is switched off and the total amount of hydrogen produced by PEMWE is sent to the storage. Instead, when it is higher than the previous threshold and there is hydrogen production, an amount produced is sent to FPP to work at minimum load condition, and the remaining goes to the storage. When the hydrogen storage is almost full (the storage level is higher than a fixed threshold), and there is no power surplus, the storage level decreases supplying hydrogen at the FPP working at minimum load conditions.
- Final product plant: the management of the FPP, independently of the type of process considered, consists of the aim of keeping them in on status, at least at minimum load capacity. The FPP strategy tries to avoid the continuous switch on/off

of this component. More specifically, the FPP works at minimum load when the storage is not in full condition or when the surplus power from the grid is null and the FPP is already in function. It works from minimum to nominal load when the storage is full depending on the power surplus. Instead, when the storage level is lower than a minimum threshold, it is switched off.

The global strategy is synthetised in *Figure 3.12*.

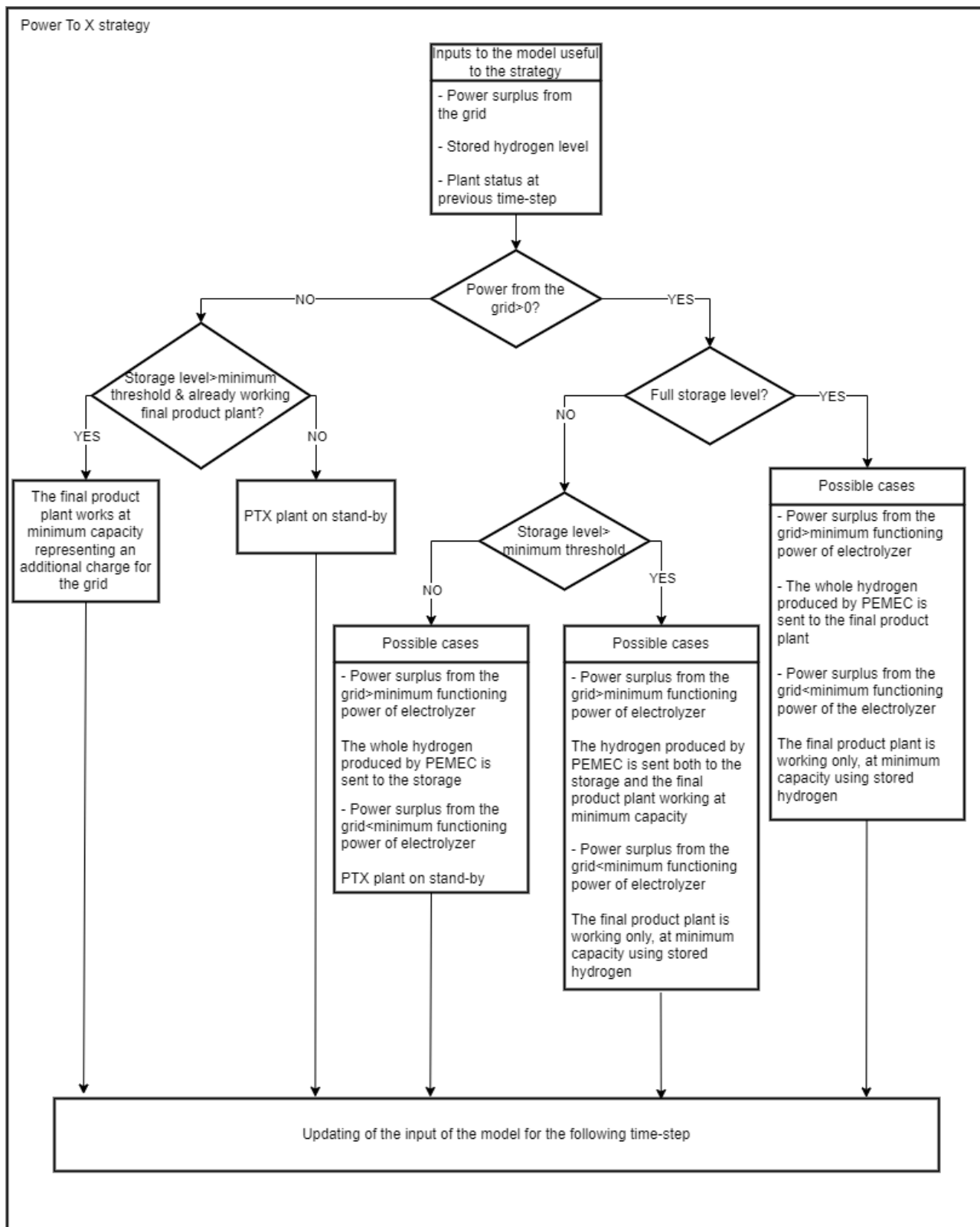


Figure 3.12 Block diagram of the PtX model strategy

4. Validation and comparison of the of the PtX models

To evaluate the reliability of the built models, the three different PtX plants are simulated in a daily scenario with RES penetration of 30% referred to January period. The aim is to ensure that the PtX consumption profile strictly follows the surplus power available from the grid respecting the strategy constraints. The simulations are performed considering:

- the PtX plants installed in the same grid node (node 62);
- the PEMWE sizes set to 4 MW;
- the reference day at 8th of June;
- the time step equal to one minute;
- the PtX typology as the only variable that changes.

The results (*Figures 4.1-4.2-4.3*) show that all the PtX have a good response to the power surplus oscillations allowing to properly follow the input power at the plants. So, for the same power surplus profile, it can be highlighted that the methane, syngas and, methanol plants are initially in idle conditions, since there is no power surplus available from the grid. Then when the power surplus overcomes a minimum threshold, which varies with the nominal PtX power, the PtX starts to follow the power profile up to a certain power (that depends on the hydrogen storage level and the nominal power of the plant). At the same way, when the power profile decreases, the plant continues to follow it until it reaches the minimum power threshold. Then the PtX power absorbed is constant and represents the power needed by the FPP working at a minimum load condition.

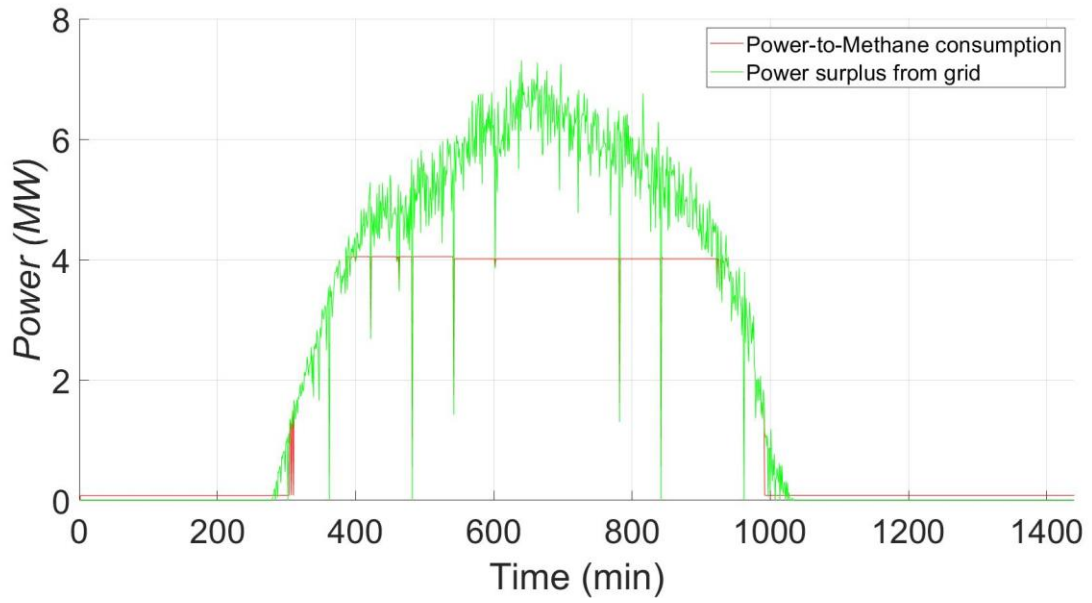


Figure 4.1 Power-to-Methane power absorption profile

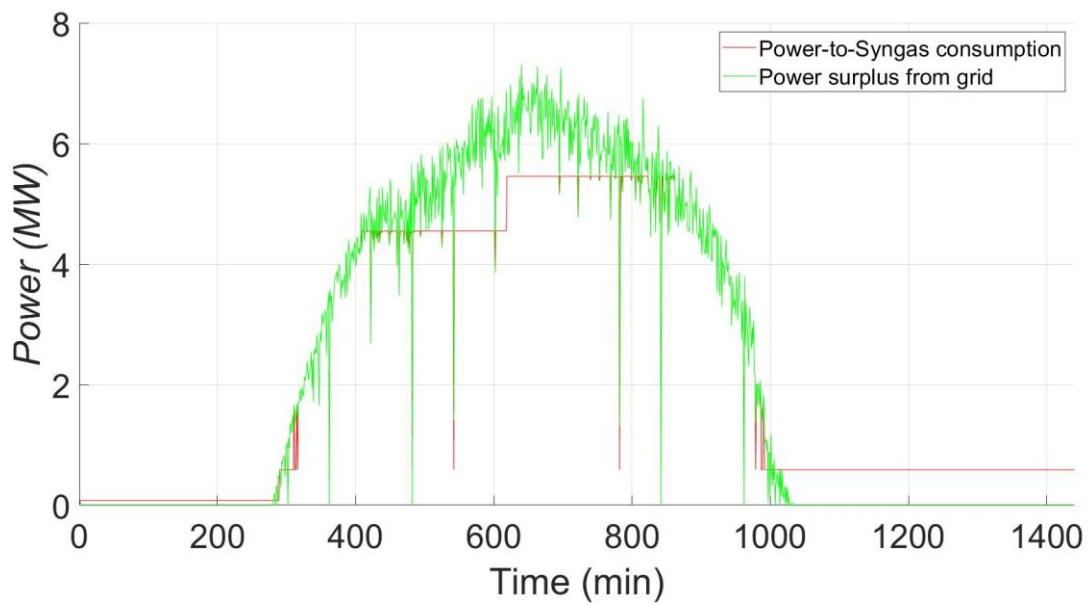


Figure 4.2 Power-to-Syngas power absorption profile

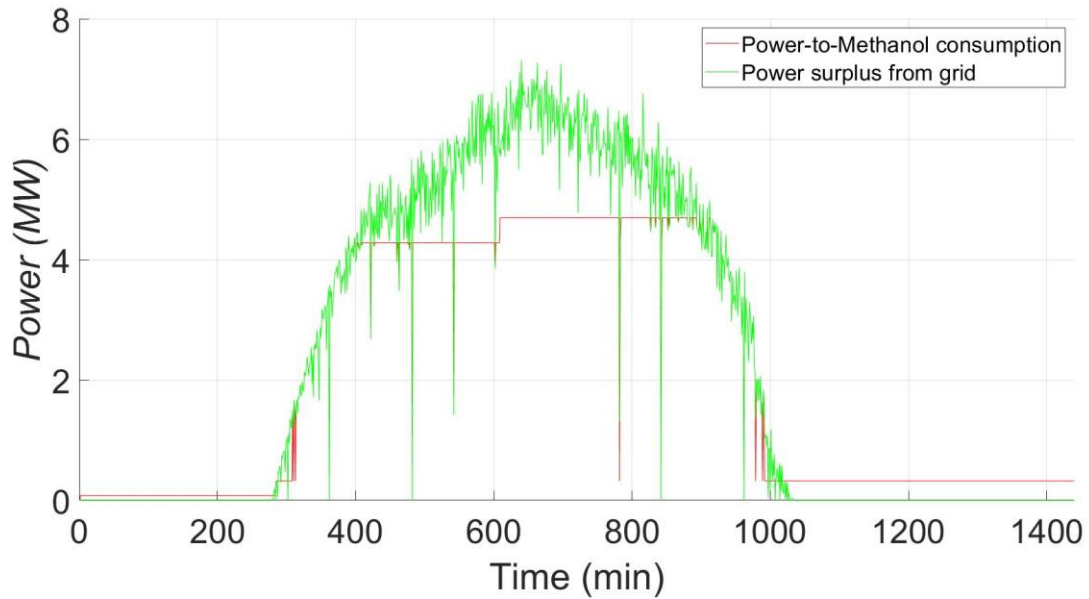


Figure 4.3 Power-to-Methanol power absorption profile

Looking the three graphs in detail, it is important to underline the similarities and the differences. In particular, the idle condition (timestep<300 minutes) is the same for the three PtX. However, the two plateaus differ among the PtX that can be observed when the power surplus reaches the highest values (450 minutes<timestep<850 minutes). For the methane plant, the first and the second plateau are quite similar reaching the value just over the PEMWE installed power. For the syngas plant, the first plateau is close to 4.5 MW, while the second one to 5.5MW. The methanol plant has a plateau at 4.25MW and a second close to 4.75MW. The common point of the PtX is that the plateaus are observed when the power surplus overcomes the power absorbed by the plants. The power surplus is not the only parameter that affects the plateaus. Indeed, the hydrogen storage level also differentiates the two plateaus. The first is reached when the storage is not already full; in fact, the power absorbed by the PtX is represented by the sum of the nominal power of the electrolyser, the power needed from the FPP working at minimum load condition, and the power needed to compress and store the residual hydrogen produced. The second one is reached when the hydrogen storage is full and the PtX consumption is equal the sum of the electrolyser nominal power and the power absorbed by the FPP at nominal condition. Regarding what discussed above, the values of the PtX plants plateaus differ due to the divergent FPP plants nominal consumptions. For the same reason, the starting and ending points of the plateaus also differ among the PtX. Indeed, the Power-to-Methane plant reaches sooner the plateau, and leaves this condition, compared to the other to PtX plants, later. Another interesting

aspect to consider is that for the syngas and methanol plants, the first plateau is lower than the second one, while for the methane, is the opposite. This means that for the Power-to-Methane plant, the hydrogen compression is more expensive from the energy point of view, with respect to the FPP consumption.

The last aspect to be noted is the consumption when the grid power surplus goes to zero (timestep>1000 minutes). Since the hydrogen storage is full, the FPP plants continue to work at minimum load capacity. Looking at the three figures, it is evident that the power absorbed in this period differs among the PtX considered. The lowest FPP power absorbed is represented by the methane plant, while the highest, by the syngas plant. These power absorption values are function of the type of process, and the global exothermicity and endothermicity of the reaction. As we will see in detail in Chapter 6, this aspect deeply affects the capacity factors of the plants.

Then the hydrogen storage profile of the only Power-to Syngas is reported in *Figure 4.4*, to correlate the PtX consumption with its functioning.

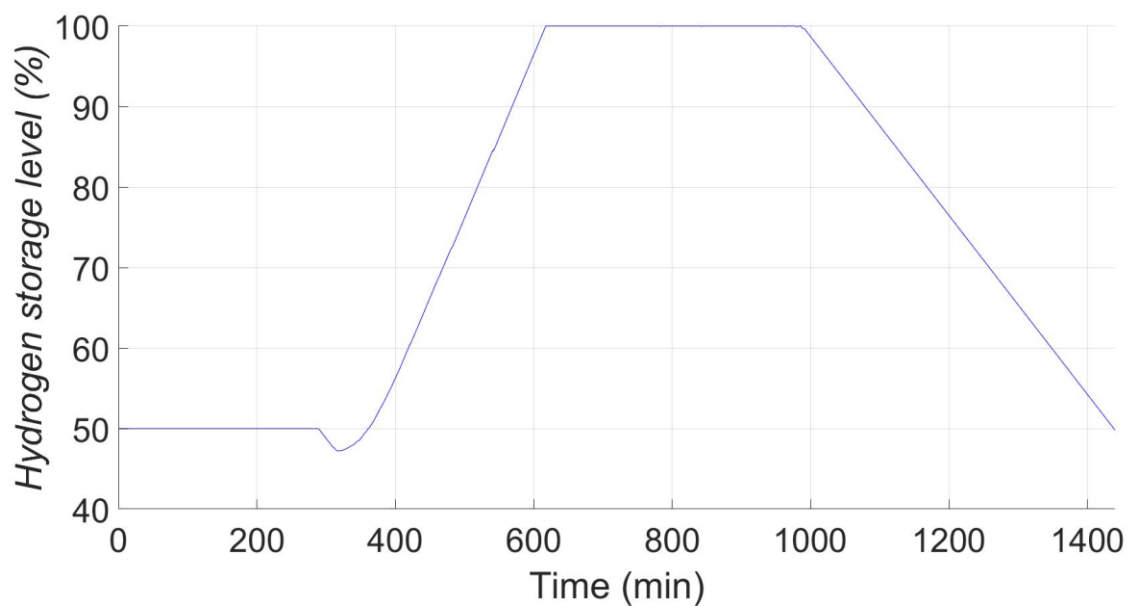


Figure 4.4 Hydrogen storage level – Power-to-Syngas model validation

Since there is no input power at the PtX and both the PEMWE and the FPP are switched off, it can be observed that the hydrogen storage level is constant until minute 290. Later, the profile is decreasing because the PtX is supplied from the grid with power surplus, but the moles absorbed by FPP (working at minimum capacity) are higher than the ones eventually produced by the PEMWE. When the power surplus from the grid increases, the

hydrogen profile is crescent since the PEMWE works at a higher load. So, the moles of hydrogen produced exceed the amount required by the FPP. Around minute 620, the storage reaches the full condition and it lasts until minute 980. In this period, all the hydrogen produced is sent completely to the FPP. From minute 980 to the end of the day simulated, the hydrogen storage level decreases constantly. In this phase, the sudden reduction up to zeroing of the power surplus leads to the activation of the only FPP that works with a constant hydrogen flow rate drawn from the hydrogen storage.

Combining the discussion done on the hydrogen storage profile and the Power-to-X power absorption, it is possible to emphasise that the mainly differences among the models are related to the response time of the plants. Indeed, for the Power-to-Methane and Power-to-Methanol plants, the storage profiles have the same trend with the only differences in the time at which the storages start to discharge and then to charge, the time at which they are completely filled, and the minute at which the hydrogen level starts to decrease.

5. Cases of study

The goal of this dissertation is to evaluate how the installation of the several PtX plants impacts the operation of the electric grid. Clearly, the impacts and the results are influenced by the scenario considered and the initial conditions set. The scenarios take into account the reference periods, the electric grid characteristics, the PV generation profiles, the load profiles, the number of PtX installed and their location on the grid, the typology of the PtX and their sizes, the initial hydrogen storage level, and the time step of the simulation.

Starting from the reference periods, these are represented by a week in January (from 8th to 15th) to simulate the winter working conditions, and a week in June (from 8th to 15th) to simulate a spring/summer scenario. For what concerns the time step, it is assumed to be equal to 1 minute considering the plants at the stationary level. So, 10080 iterations are performed for each simulation.

The electric grid parameters and the nodal loads are the ones defined in paragraph 2.1. The PV generation profiles are considered as the result of the PV penetration coefficient. A first scenario is simulated at 30% of the PV share and at 50% in the second one, both with respect to electric load of the grid in January. These PV penetrations are obtained as the ratio between the energy supplied by the PV plants and the total absorbed energy by the loads.

Considering the sizes and the installation nodes of the PtX plants, they are kept constant from the previous study [12] for all the simulations and are reported in *Table 5.1*.

Table 5.1 PtX installation nodes and sizes [12]

Installation node	PtX size (MW)
11	2
123	2
62	4
57	3
100	2
97	1
107	2
95	3
117	3
112	3
120	4
130	3
127	4
126	3
146	2
9	2
149	3
145	3

The PtX typology is the parameter changed to simulate the three different plants. Note that for each simulation, the typology is assumed to be equal to one value for all the installation nodes, so all methane or methanol or syngas plants are installed and simulated.

The last assumption done in the model regards each PtX hydrogen storage: the storages are initialised to a hydrogen level of 50%.

Then having defined the load and PV generation at the nodes, the resulting power surplus at the PtX installation nodes can be evaluated. In *Figure 5.1* and *5.2*, the power surpluses

of the first scenario (PV penetration 30%) at the first PtX plant (node 11) for the two-reference periods are shown.

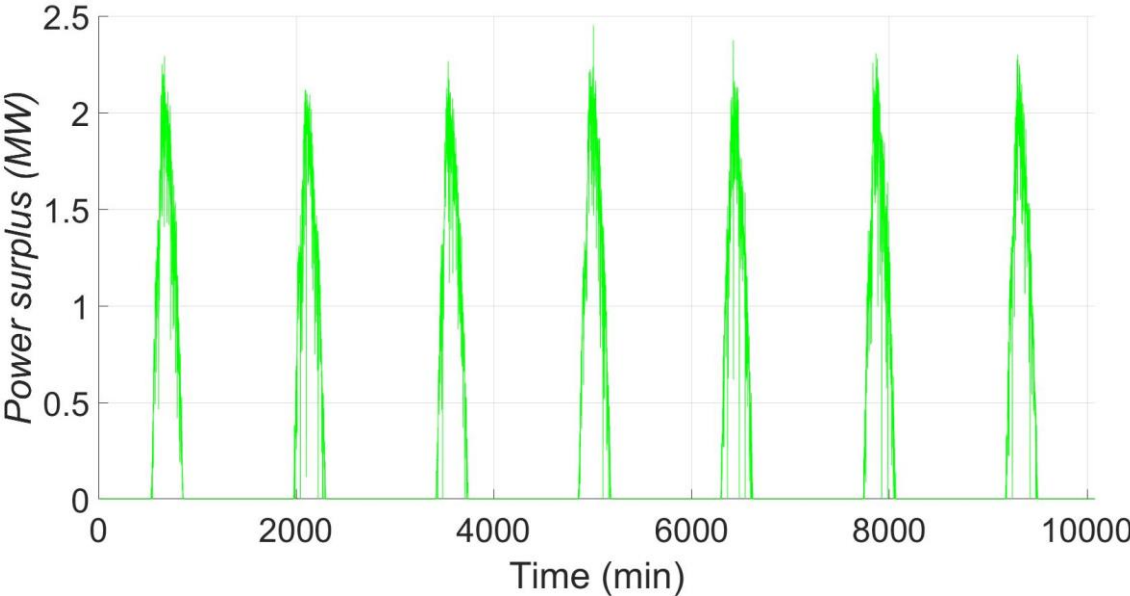


Figure 5.1 Winter power surplus at node 11 for 30% of PV share

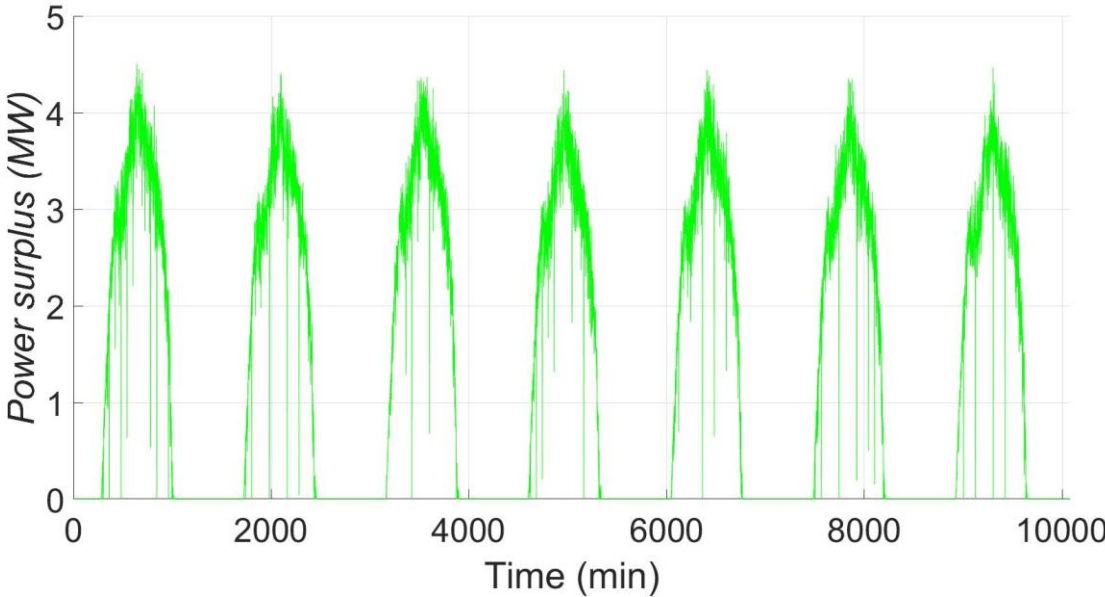


Figure 5.2 Summer power surplus at node 11 for 30% of PV share

The main differences that can be highlighted between the winter and summer power surpluses are the peak values and the time extension of the surplus availability. In the winter week, the peaks reach the maximum value of 2.3 MW, while, in the summer week, 4.5 MW. The time availability in a day of the surplus power in the former case is around 350 minutes, whereas, in the latter is about 750 minutes.

For the second scenario, both for the winter (Figure 5.3) and summer (Figure 5.4) period, the power surplus reaches higher peaks values than the first scenario. Also, the time extension of the power surplus is wider than the previous case study. Since the loads profiles of the grid are considered always constant, the variation of the power surplus profile in the second scenario is due to the increment of the PV generation.

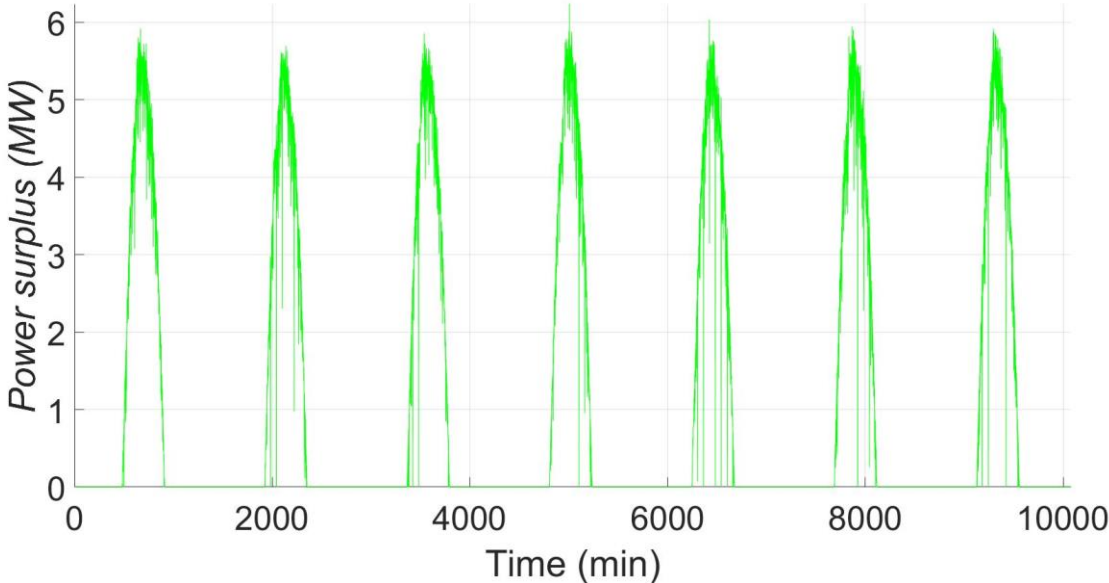


Figure 5.3 Winter power surplus at node 11 for 50% of PV share

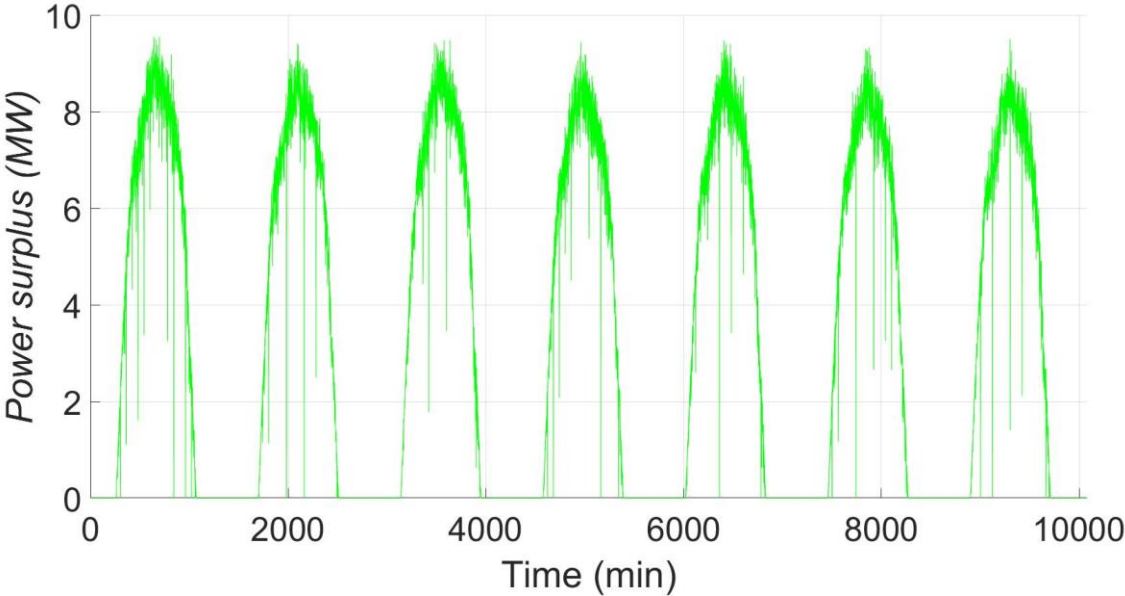


Figure 5.4 Summer power surplus at node 11 for 50% of PV share

These huge power surplus variations, together with the differentiation of the PtX installed and the reference periods, allow to simulate a wide range of possible working conditions.

To sum up, the common parameters, considered constant for all the simulation, are the electric grid structure, the PtX sizes and installation nodes, the loads profiles, and the initial H₂ storage level. Instead, the parameters changed are the reference periods, the PtX typology and the PV penetration level leading to the simulation of 12 cases. As a result, the analysis of the models simulations outcomes gives a feedback on how much each of the many defined variables affect the calculations.

6. Outcomes of the model

In this section the most relevant outcomes of the Power-to-X simulations are reported. These are related both to the functioning of the electric grid (like the reverse power flow impact, the energy losses, the nodal voltages, and the branch currents) and to the PtX plant itself (capacity factor, embedded CO₂ and process efficiency). The results are discussed in depth in the next paragraphs, but it is worth anticipating that each Power-to-X outcome is deeply affected from the scenario considered and the differences between the initial and final hydrogen storage level.

6.1 Reverse Power Flow

Among the several electric parameters, the impact of the installed PtX plants on the electric grid is quantified by the evaluation of the RPF phenomenon. In detail, for each simulation, both RPF and the time duration of the phenomenon are evaluated. The results of the three different PtX for the two reference periods and a PV penetration of 30% are shown in *Table 6.1*.

Table 6.1 Reverse Power Flow for 30% of PV share

Reference period	Simulation settings	RPF (MWh)	Variation (%)	Minutes of RPF	Variation (%)
Winter	Without PtX plants	407.2	/	1934	/
	With PtX plants	0.00	-100	0	-100
Summer	Without PtX plants	2561	/	4849	/
	Power-to-Methane	2.30	-99.9	89	-98.1
	Power-to-Syngas	0.00	-100	0	-100
	Power-to-Methanol	0.07	-99.9	7	-99.8

As expected, before the PtX plants installation, the RPF phenomenon occurs more frequently in the summer reference period since the PV production is much higher than the winter period. Indeed, the amount of RPF during the summer week is more than six times the one transferred in the winter week. As a consequence, also the time duration of the phenomenon differs. In the winter season, the RPF takes place around the 19% of the simulated period, while in the summer around the 48%.

After the PtX installation, during the winter week the RPF issue is completely solved regardless of the type of PtX considered. In the summer reference period, the RPF phenomenon is absent only with the installation of Power-to-Syngas plants. For the other two types of PtX, the RPF is almost entirely solved.

The outcomes (shown in *Table 6.2*) of the simulations take into account the PV penetration level of 50%.

Table 6.2 Reverse Power Flow for 50% of PV share

Reference period	Simulation settings	RPF (MWh)	Variation (%)	Minutes of RPF	Variation (%)
Winter	Without PtX plants	2038.5	/	2837	/
	Power-to-Methane	245.16	-88.0	1356	-52.2
	Power-to-Syngas	84.70	-95.8	792	-72.1
	Power-to-Methanol	157.33	-92.3	1114	-60.7
Summer	Without PtX plants	6991.9	/	5523	/
	Power-to-Methane	2973.8	-57.5	4404	-20.3
	Power-to-Syngas	2105.5	-69.9	4127	-25.3
	Power-to-Methanol	2552.8	-63.5	4302	-22.1

It is worth noticing that comparing the cases without the PtX reported in *Table 6.2* with the ones reported in *Table 6.1*, the RPF is steeply increased. For the winter period, the RPF for the high PV penetration is 5 times the RPF calculated for the lower PV penetration. Whereas, in the summer reference period and for 50% of PV, the reverse energy is 2.7 times the one evaluated for the 30% PV case.

In the high PV penetration scenario, the differences between the three PtX are evident. Indeed, it can be observed that in both the reference periods, the Power-to-Syngas plants minimise the RPF issue, resulting in the best option. Nevertheless, the RPF is not completely reduced to zero even in the best cases. In fact, in the winter reference period, for the Power-to-Syngas plants, the RPF is reduced of the 95%, while in summer, of the 70%.

To further reduce the RPF issue, especially for high sharing of PV generation, two solutions can be considered both aiming at increasing the total PtX load installed:

- the installation of more PtX plants keeping their size lower than 4 MW.
- The increase of the already installed PtX plants sizes.

It can be assumed that the first solution has an economic drawback, as by raising the number of plants installed both the capital and the operating expenditure increase. The second solution has a worse impact of big loads on the grid functioning as its main drawback. Due to the relevant voltage drop at the PtX installation node, an undervoltage can occur. Additionally, overcurrent issues in the branch having a small load capacity can happen too.

6.2 Grid losses

The second outcome related to the electric grid refers to the grid losses. These are dependent to the branch impedance and the current which flows along the grid. The high currents inside the branches are due to the increment of loads on the grid or the RPF generated at high PV share. The losses can be evaluated through the application of the Ohm law.

In *Table 6.3* the cumulated energy losses along the grid for the RES penetration of 30% are shown. It can be highlighted that in the cases without PtX installation, the energy losses are

higher in the summer period than the winter one. The reason behind this difference is the RPF which reaches higher value when there is excessive PV production and low load absorption. It has to be specified that a low PV penetration that avoids the reverse power flow phenomenon, is beneficial for the grid since it reduces the losses of energy. This is because a distributed energy generation allows to supply, and, so, to match the loads locally. The benefit derives from the reduction of the pathway that the energy has to take from the generator to the load.

The installation of the PtX plants in the winter period has a slightly negative effect since, despite their installation removes the RPF, during the nights the absorbed power by the plant represents an additional load for the grid. Instead, in the summer reference period, the PtX installation has a relevant positive influence. In fact, all the three models simulated enable the reduction of the grid losses. In particular, the reductions are due to the great reduction of the RPF (in absolute value) that overclass the negative impact of the night functioning of the plants on the losses reduction. The Power-to-Methane plants represent the best option from the energy losses variation point of view, in both the reference period. Specifically, in the winter season, it has the smallest increase of the losses, while in summer has the highest losses reduction.

Table 6.3 Grid losses for 30% of PV share

Reference period	Simulation settings	Grid losses (MWh)	Variation (%)
Winter	Without PtX plants	47.48	/
	Power-to-Methane	47.83	+0.74
	Power-to-Syngas	48.92	+3.03
	Power-to-Methanol	48.52	+2.19
Summer	Without PtX plants	52.78	/
	Power-to-Methane	34.73	-34.2
	Power-to-Syngas	40.22	-23.8
	Power-to-Methanol	37.18	-29.6

The grid losses for a PV penetration equal to 50% are reported in *Table 6.4*. In this scenario, due to high RPF, the simulations without any PtX installed show higher energy losses than

the ones shown in *Table 8*. In both the reference periods, all the types of PtX installed reduce the grid losses. To summarise, the losses calculated are a trade-off between the positive effect on the reduction of the RPF and the negative impact of the night working condition of the plants that further overwhelms the electric grid. For a 50% of PV share and the winter period, the Power-to-Methane plants installation maximises this trade off (grid losses reduced of around 20% compared to the initial case), while for the summer simulation it is the Power-to-Syngas installation (grid losses reduced of around 47% compared to the initial case).

Table 6.4 Grid losses for 50% of PV share

Reference period	Simulation settings	Grid losses (MWh)	Variation (%)
Winter	Without PtX plants	63.89	/
	Power-to-Methane	51.20	-19.9
	Power-to-Syngas	54.66	-14.4
	Power-to-Methanol	52.68	-17.5
Summer	Without PtX plants	135.29	/
	Power-to-Methane	76.45	-43.5
	Power-to-Syngas	72.54	-46.4
	Power-to-Methanol	74.06	-45.3

6.3 Nodal voltage and branch current

In addition to the study of the RPF phenomenon and the energy losses, the nodal voltages and the branch currents are checked. As already expressed in chapter 2.1, the increase of the RES generation on the electric grid could determine the occurring of overvoltage and overloading that should be avoided. At each time step, the voltages and the currents are obtained from the backward and forward sweep algorithm. To simplify the data analysis, during the simulations at each node of the grid, only the maximum and minimum voltage level are reported to evaluate possible overvoltage. Instead, regarding the overloading, the maximum branch currents are shown.

Starting from the overvoltage analysis, the voltage data (expressed in p.u.) related to scenarios with 30% and 50% of PV penetration and the two simulation periods are shown in Figures 6.1-6.2-6.3-6.4.

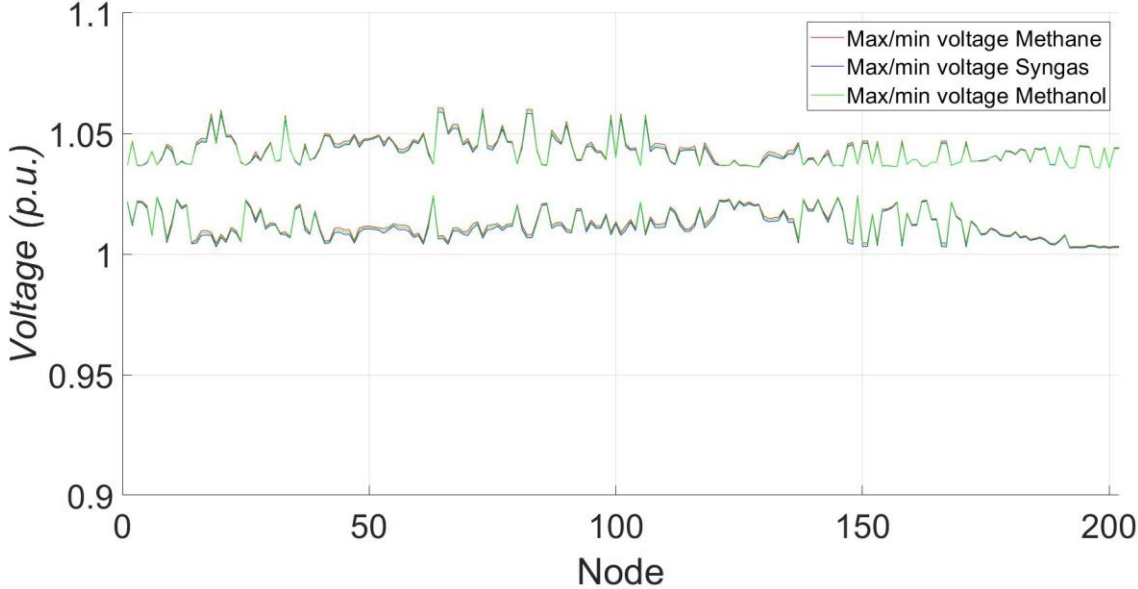


Figure 6.1 Maximum and minimum voltage profile in winter scenario with 30% of PV share

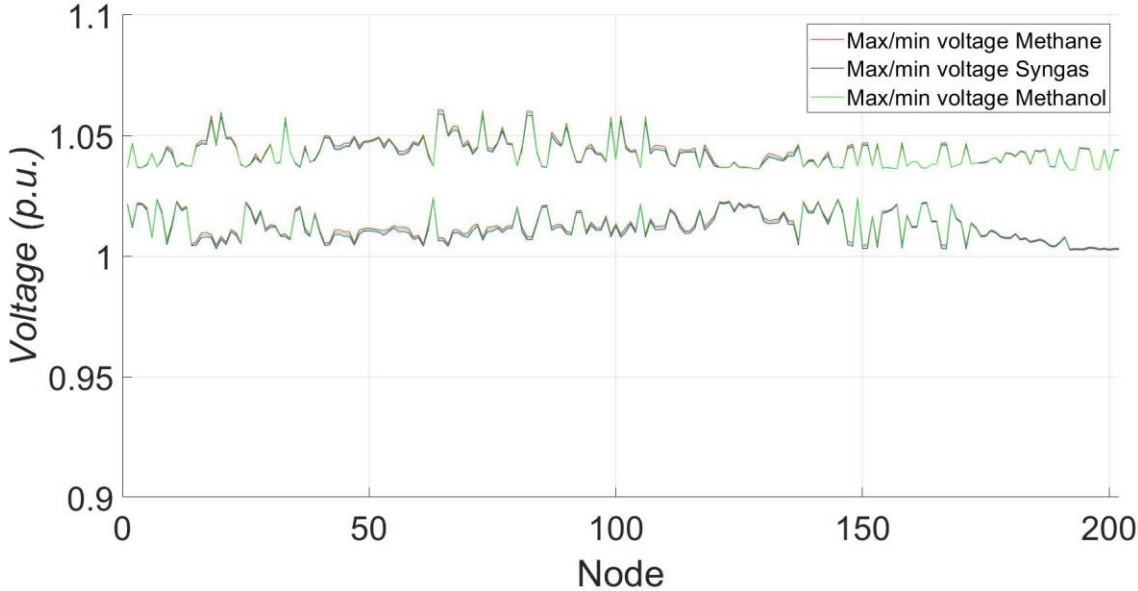


Figure 6.2 Maximum and minimum voltage profile in summer scenario with 30% of PV share

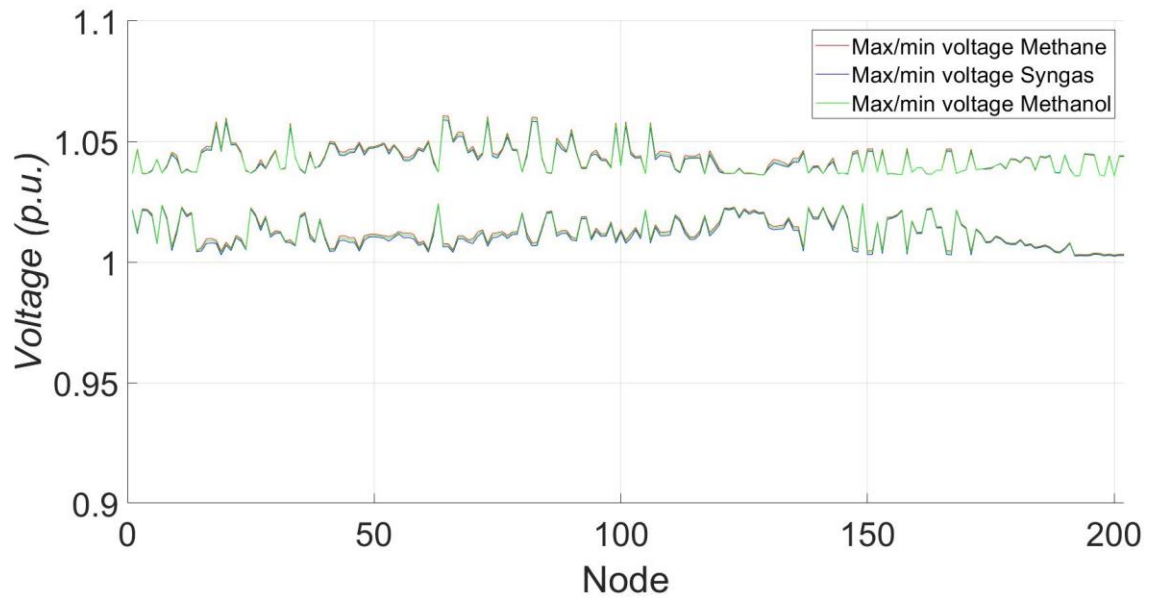


Figure 6.3 Maximum and minimum voltage profile in winter scenario with 50% of PV share

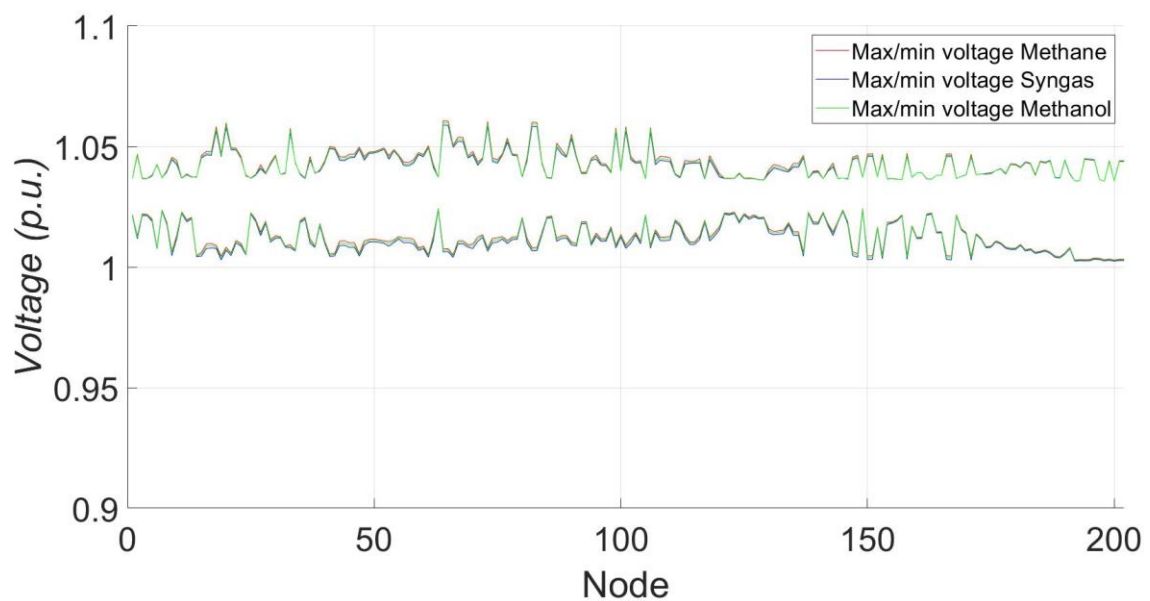


Figure 6.4 Maximum and minimum voltage profile in summer scenario with 50% of PV share

The first thing to observe is that in all the scenarios, there are neither overvoltage nor undervoltage. Indeed, the node voltages are within the maximum value of 1.1 p.u. and the minimum of 0.9 p.u.. The second thing is that the maximum voltage profile increases when the local generation is higher, and it is more visible comparing the *Figures 6.2* and *6.4*. So, as expected, the highest voltage levels are reached in the summer scenario with 50% of RES penetration. Not relevant differences are detected among the three PtX models.

For what concerns the overloading issue, the maximum branches load experienced during the simulations are reported in the *Figures 6.5-6.6-6.7-6.8*. First of all, the maximum current flows are quite similar among the three typologies of PtX. The figures show large oscillations between the several branches, meaning that some branches are more loaded than others. Another common consideration is that the branch currents in the summer period are higher than the ones of the winter periods. For the scenario with lower PV penetration, the currents inside the branches do not reach their maximum limit. More specifically, the maximum branches load for these simulation cases reach values of 75% of their limits.

For the higher PV penetration, the currents limits are not always satisfied. In the winter week, the limits are slightly exceeded (101% and 103%) by two branches for one time step, so one minute. Since the small-time extension and magnitude of the phenomenon, it could be assumed that the branches could withstand to the thermal stress generated.

Different considerations have to be done on the results during the week of June. In this time frame, the overcurrent issue cannot be neglected since it assumes a significant weight. Twelve branches are affected by this issue and the highest branch overload is equal to 151%. A possible solution to reduce the overcurrent phenomenon could be changing the conductors, by increasing their size.

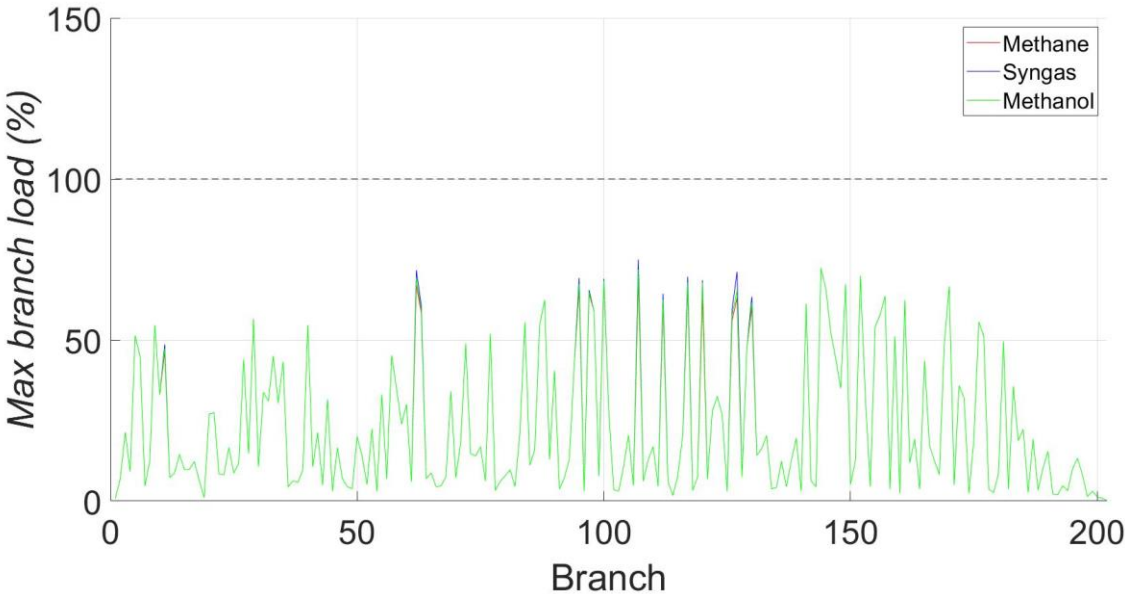


Figure 6.5 Maximum branch load in winter scenario with 30% of PV share

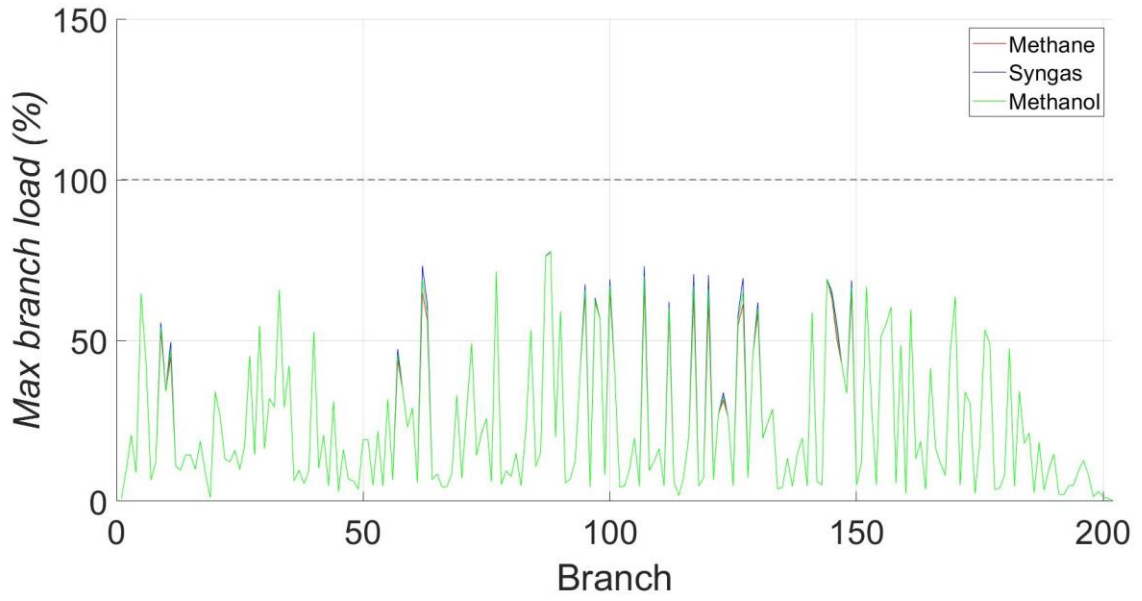


Figure 6.6 Maximum branch load in summer scenario with 30% of PV share

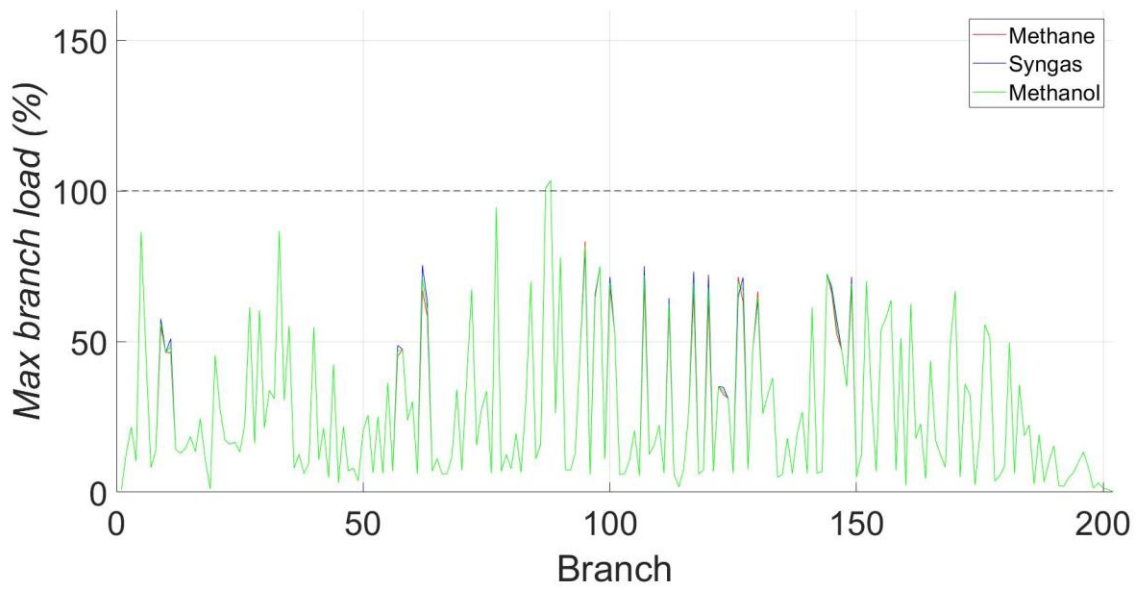


Figure 6.7 Maximum branch load in winter scenario with 50% of PV share

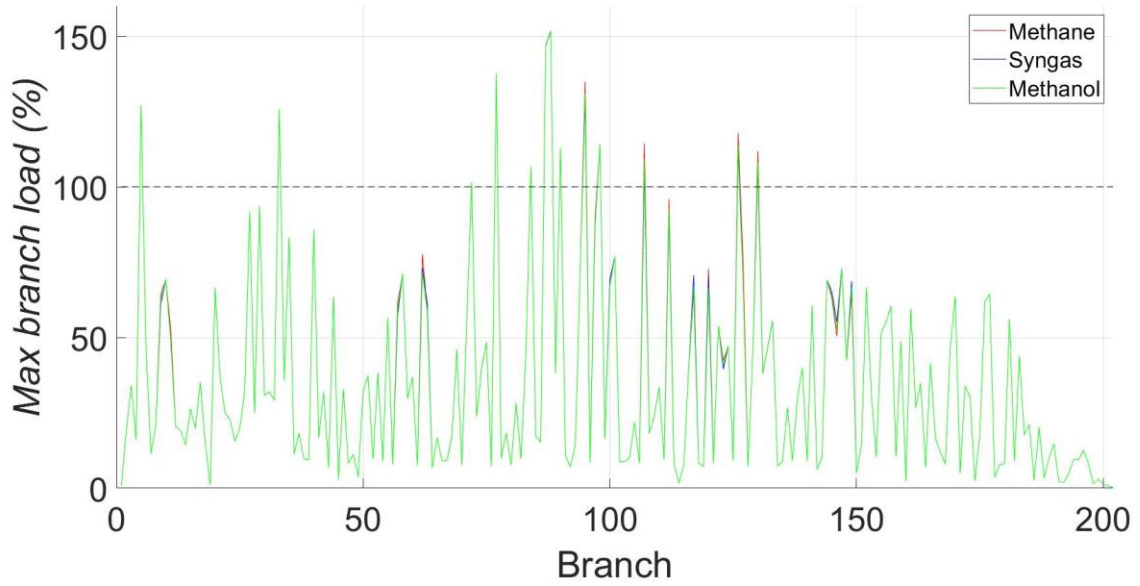


Figure 6.8 Maximum branch load in summer scenario with 50% of PV share

6.4 Capacity factor

Another result calculated for each PtX plant is the capacity factor. The capacity factor represents a measure of the relationship between the amount of energy a plant absorbs and the amount it could absorb, if it operated at its nominal condition. In other words, the capacity factor quantifies how much the installed plant is exploited with respect to its maximum. It is a dimensionless value that can vary between 0 and 1.

In this study, the capacity factor is evaluated with the *Equation 6.1*.

$$CF = \frac{E_{absorbed}}{P_{plant\,nominal} \cdot R_{time}} \quad (6.1)$$

At the numerator, the effective amount of energy absorbed by the PtX plant in the simulated period (R_{time}) is reported. While, at the denominator, there is the energy that would be absorbed by the PtX plant if it worked at nominal condition. This last term is obtained by the product of the nominal power of the plant and the reference period. More specifically, the nominal power of the plants is represented only by the PEMWE power installed for the Power-to-Methane and the Power-to-Methanol plant (exothermic reaction). Conversely, for the Power-to-Syngas, due to the endothermicity of the reaction, the nominal power is

obtained by the sum of the PEMWE and the heat needed for the syngas synthesis. So, for the same PEMWE size installed, the denominator of the ratio for the Power-to-Syngas is higher than the ones of the Power-to-Methane and Power-to-Methanol, whereas, the numerator depends both on the working time and functioning points of the plant.

Starting from the winter week and a PV penetration of 30%, the capacity factors of the different PtX plants are shown in *Figure 6.9*.

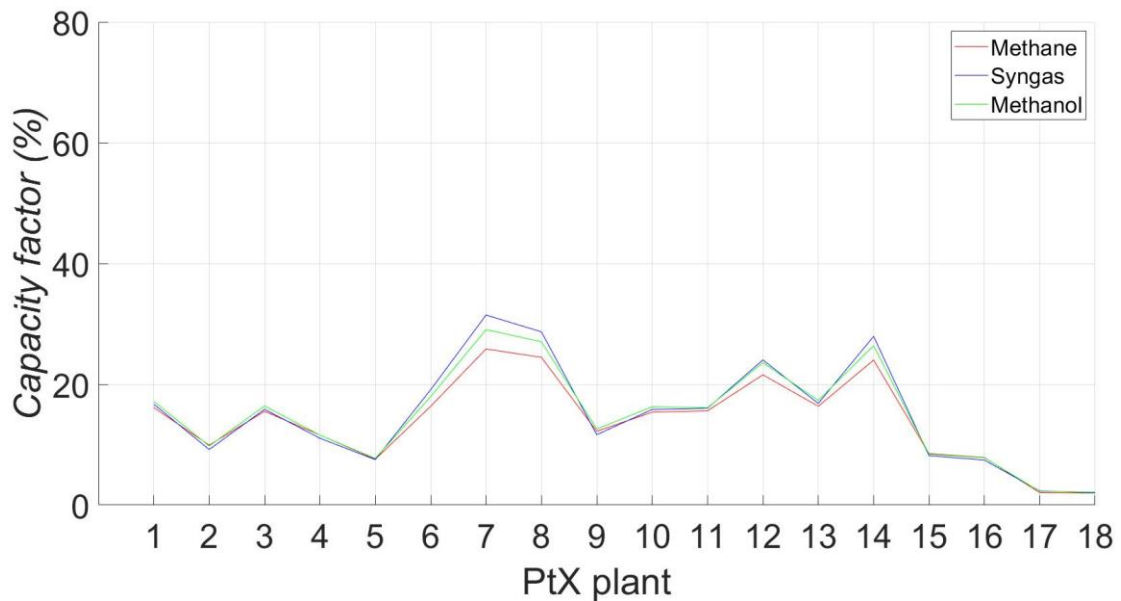


Figure 6.9 PtX capacity factors in winter scenario with 30% of PV share

In this scenario, one of the limits of these plant, so their low capacity factors, must be highlighted. The differences among the three kinds of plants can be neglected; indeed, the average capacity factor values of the methane, syngas and methanol, are respectively 14.06%, 15.10% and 14.98%. These low values are due to small amounts of power surplus given as input to the PtX, because for, most of the time the plants are switched off. Furthermore, only for a few times, the FPP works as an additional load when there is no power surplus and the H₂ storage full. It is clear that these outcomes are a weak point of the analysis; in fact, an under-exploitation of the PtX plants could represent a not well weighted investment compared to the benefit achieved. Though, it must be said that the capacity factors reported refer to the worst working period of the year, and in order to have a clear information on how much the PtX plant will be exploited, a wider analysis has to be performed.

Thanks to the implemented strategy, the night functioning of PtX affects the capacity factors. Due to the several distinctions of the models, the number of night functioning varies among the three types of plants. In detail, the times that the plants work when there is no power surplus are reported in *Table 6.5*.

Table 6.5 FPP night working times per week in winter scenario with 30% of PV share

Installation node	Power-to-Methane (times/week)	Power-to-Syngas (times/week)	Power-to-Methanol (times/week)
11	3	1	2
123	1	0	0
62	2	1	2
57	2	0	0
100	1	0	0
97	4	2	2
107	4	4	4
95	5	4	4
117	2	0	1
112	4	1	2
120	2	1	2
130	4	2	4
127	3	1	2
126	4	4	4
146	1	0	0
9	0	0	0
149	0	0	0
145	0	0	0

The Power-to- Methane plant is the kind of model that works the most when there is no power surplus. From the table above, the 18 Power-to-Methane plants work 44 nights over a maximum of 126 in a week, the Power-to-Syngas 21 and, Power-to-Methanol 29. This is a consequence of the PtX nominal power installed. It is known that a reduction of the plant

power installed leads to an increment of the working period of the plant itself. Among the three models studied, for the same PEMWE size installed, the Power-to-Methane has the smallest total power installed, while the Power-to-Syngas, the highest. From this analysis the Power-to-Methane works more during the day when there is power surplus. This condition allows to fill sooner the hydrogen storage, so, unlocking the possibility to keep working with the FPP. Despite the Power-to-Methane plants works more than the other two PtX, their capacity factors are lower than the ones of the other PtX plants. This depends on the different weights that FPP have compared to the total PtX plant. The Power-to-Methane, indeed, has the lowest FPP power installed among the three PtX. Thus, the weekly final PtX consumptions are the lowest for the Power-to-Methane and the highest for the Power-to-Syngas.

In addition to the analysis done, a common hydrogen storage profile of the scenario simulated is reported in *Figure 6.10*. It is relevant to note that, referring to the Power-to-Methane plant in winter season with low PV penetration, the plant has to work two days to fill up to 90% the hydrogen storage. Once reached that condition, a huge drop of the storage level can be observed. These drops represent the hydrogen drawn to feed the FPP that works at minimum capacity during the night.

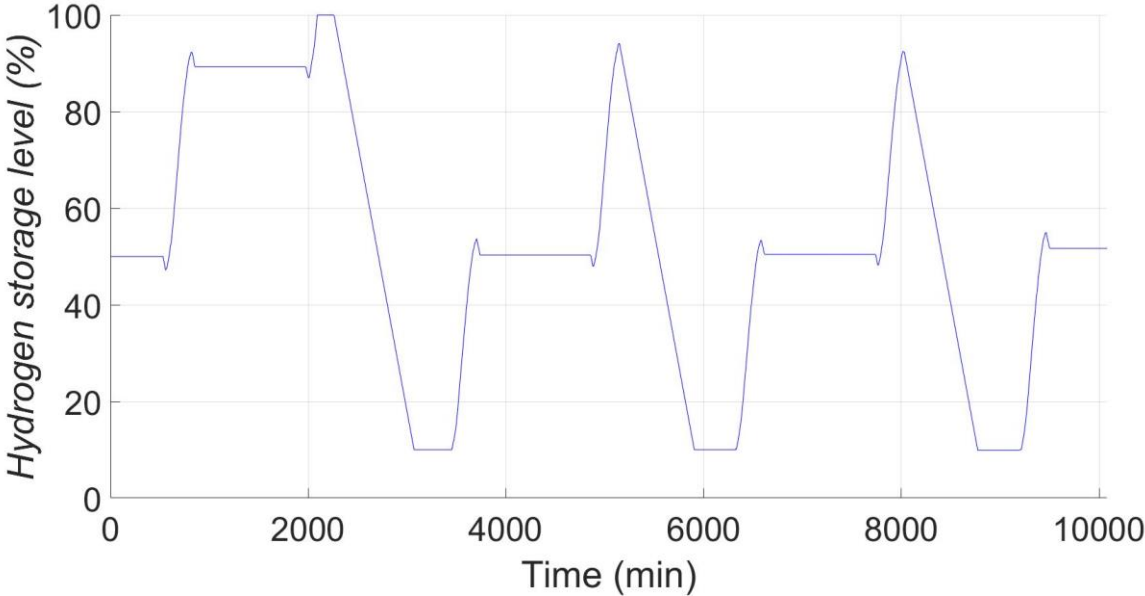


Figure 6.10 Hydrogen storage level in winter scenario with 30% of PV share (Power-to-Methane installed at node 11)

Likewise, for the same PV penetration scenario, in the summer reference period, the capacity factors study is performed. Looking at *Figure 6.11*, two main assessments can be done. The first one is that the capacity factors reach higher values than the previous reported. The second one is that a relevant difference is observed among the types of PtX considered. Indeed, for the Power-to-Methane, the average plants capacity factor is 47.10%, for the Power-to-Syngas is 57.32% and, for the Power-to-Methanol is 53.04%. In this scenario, the Power-to-Syngas has the highest average capacity factor, because during the power surplus absence it absorbs the highest amount of energy. As further evidence, the energy absorbed by the FPP compared to the energy absorbed by the whole PtX plant represents the 25% for the syngas plant, the 1% for the methane plant and 15% for the methanol one.

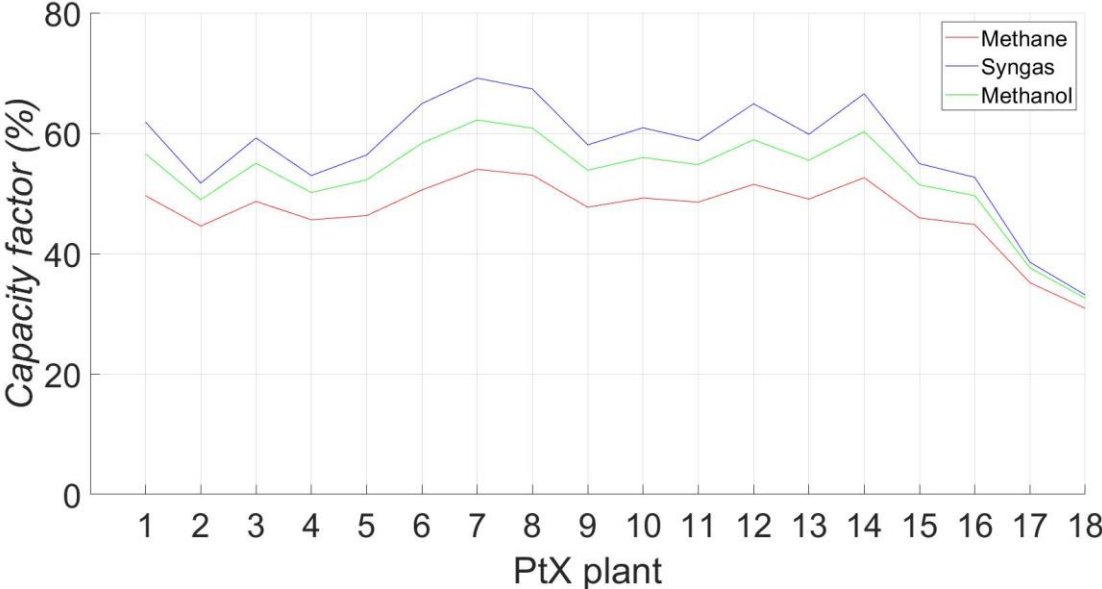


Figure 6.11 PtX capacity factors in summer scenario with 30% of PV share

Also, the analysis of a typical hydrogen storage profile (*Figure 6.12*), referred to this scenario, suggests that the FPP plants are more exploited and so affect more the model outcomes. The summer reference period allows to equalise the times per week in which the FPPs work in absence of power surplus. More specifically the FPPs of the Power-to-Methane plants are switched on 126 out of 126 nights, the syngas FPPs 119 times, and the methanol FPPs 120 times. This equalisation is due to the high PV production for a wider time availability that leads to fill the hydrogen storage during the day. The hydrogen so produced it is used as a feedstock for the FPPs in the following hours.

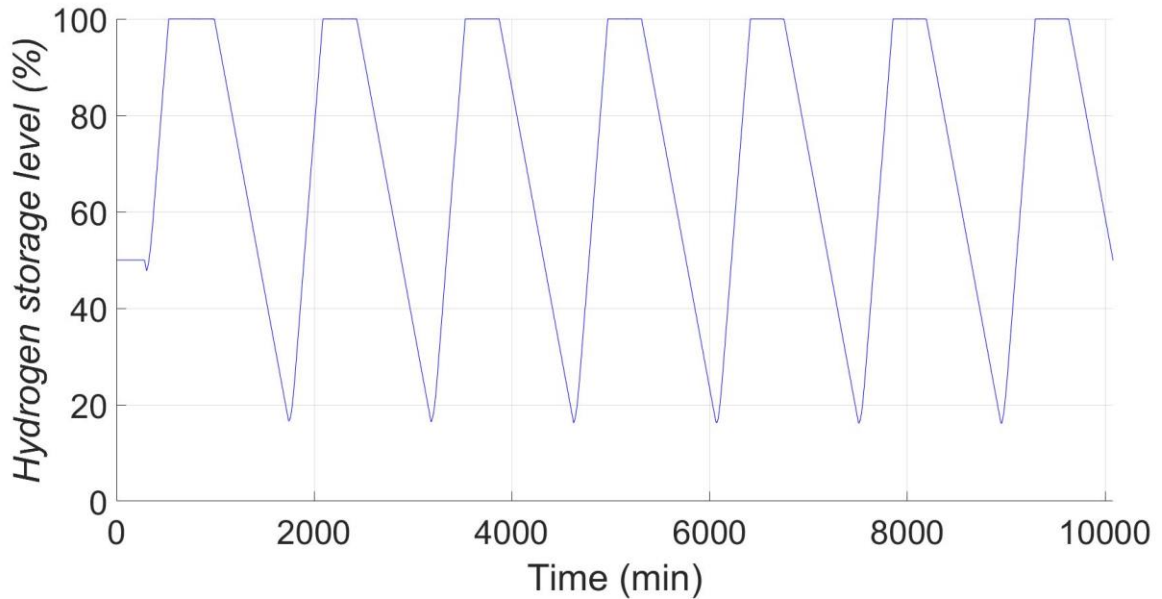


Figure 6.12 Hydrogen storage level in summer scenario with 30% of PV share (Power-to-Methane installed at node 11)

The capacity factors, both of winter and summer periods, are also reported for the scenarios with a PV penetration equal to 50% (Figure 6.13). In this case, a relevant increment of the average capacity factors can be observed compared to the 30% of PV share. Especially in the winter period, the increments are in the order of 15% for the methane plants, of 22% for the syngas plants, and of 18% for the methanol ones. The increments of capacity factors are due to the high PV penetration that allows to keep the plants in working condition during the day, thanks to the higher amount of power surplus, and to keep the FPPs in working condition all the nights. A difference between the two PV penetration scenarios is that in the lower PV penetration, the FPPs do not always work, while for the high PV penetration, the saturation of the hydrogen storage guarantees the continuous operation of FPPs. Moreover, looking at Figure 36, large variations can be spotted among the types of PtX considered in both the reference periods. In particular, the PtX plants that maximise the average capacity factors are the syngas plants since they absorb more energy during day and night. The last aspect to emphasise is the difference, for the same PtX plants, between the winter week and summer one. Since the energy absorbed at night by the FPP is quite the same in the winter and summer week, because they can be considered always switched on, the difference of the capacity factors is ascribable to the energy absorbed during the day. For sure during a winter day, the absorbed energy by the PtX is much lower than the one absorbed in a summer day.

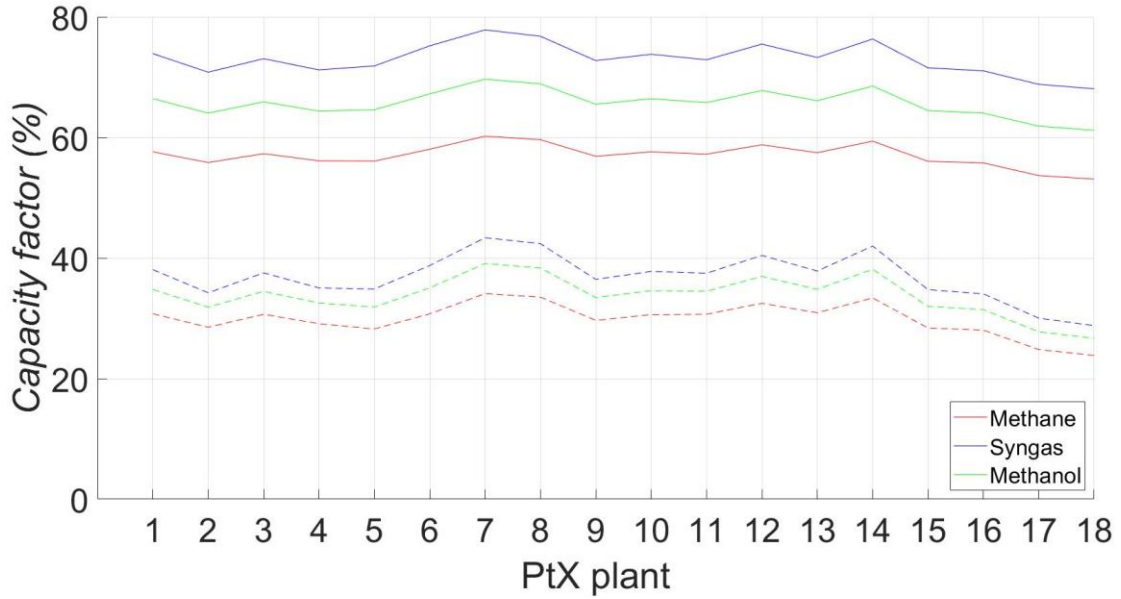


Figure 6.13 PtX capacity factors in both reference periods (dashed line for the winter and continues line for the summer) with 50% of PV share

6.5 PtX efficiency

The PtX efficiency is an additional parameter evaluated with the aim of defining how much energy absorbed by the plant is converted and stored into the products. The PtX efficiency can assume values within 0% and 100%. Equation 6.2 is implemented for the definition of this outcome:

$$EFF_{PtX} = \frac{n_{product} \cdot LHV_{product} + n_{H_2} \cdot LHV_{H_2}}{E_{absorbed}} \quad (6.2)$$

At the numerator there is the sum of two terms. The first is the multiplication of the whole amount of product synthesised during the simulation period and of the lower heating value (LHV). The LHV of the methane, methanol and hydrogen are set by literature references [23], [44]. The syngas LHV is calculated starting from the LHV of the hydrogen [23] and of the carbon monoxide [45], and the known syngas ratio equal to 2. In this way, the energy stored in the product is evaluated. The second term takes into consideration the different ending conditions of the stored hydrogen. In fact, the initial condition is the same for all the plants (initial storage level set to 50%), but the final depends on the working conditions. So, to avoid underestimation or overestimation of the PtX efficiency, n_{H_2} is calculated first. This term represents the excess/deficit of hydrogen moles compared to the initial amount

of moles stored. It is calculated as the product between the difference of the final storage level and the starting one, and the maximum number of moles of storable. Below, it is reported in explicit form (*Equation 6.3*).

$$n_{H_2} = (\%Final_{H_2} - \%Initial_{H_2}) \cdot n_{maxH_2} \quad (6.3)$$

The denominator of *Equation 6.2* represents the total energy absorbed by the PtX during the simulation period.

It must be pointed out that the results, shown in *Table 6.6*, are, however, affected by the operative working time of the FPP. The comparison among the different technologies is not useful because they work on diverse objectives and the nature of the processes are not similar.

Table 6.6 PtX efficiency for both the PV share and the simulation periods

Reference period	Simulation settings	Average PtX	Average PtX
		Efficiency, 30% PV (%)	Efficiency, 50% PV (%)
Winter	Power-to-Methane	44.31	51.49
	Power-to-Syngas	41.44	48.57
	Power-to-Methanol	38.63	45.54
Summer	Power-to-Methane	53.65	53.55
	Power-to-Syngas	50.36	50.05
	Power-to-Methanol	47.30	47.14

Looking at the single PtX typology, the efficiency varies changing both the reference periods and the PV penetration level. In particular, comparing the reference periods, it can be highlighted that, on average, the PtX efficiency is higher in the summer period than in the winter one. This can be justified considering that the equal increase of the benefit (product synthesis) and the energy consumption led to an increase in global efficiency. Analysing the same reference period for different PV penetrations it can be underlined that in the winter period, the increment of RES share increases the PtX efficiency. This growth

could be attributed to the raise of the FPPs night functioning, and, more in general, of the PtX plant. In the summer one, the efficiency can be considered almost steady.

The maximum efficiency is obtained by a Power-to-Methane plant since it has the lowest FPPs consumption compared to the amount of energy embedded in the product synthesised. The worst PtX efficiency is the one related to the Power-to-Methanol plants. In addition, it is interesting that the maximum efficiency of the PtX plants, around 54%, is a value lower than the efficiency of the PEMWE working at nominal conditions (around 63% but, it can reach higher values working at partial load as shown in *Figure 9*). Indeed, it has to be remarked that the global PtX efficiency represents the products of the efficiency of the series of processes.

6.6 Embedded CO₂ in the product

To perform an analysis of the PtX plants from the environmental point of view, the total carbon dioxide embedded in the products is evaluated. The analysis of that parameter should not be underestimated because it is related to an environmental topic, object of many current and future European and National policies. The coupling of a CC plant to a Power-to-X one is not only necessary to furnish the reactant for the synthesis of the desired product, but it could represent a key role for the future spread of these technologies. The formula applied for that evaluation is the following (*Equation 6.4*):

$$CO_{2_{embedded}} = \frac{n_{CO_2}}{E_{absorbed}} \quad (6.4)$$

n_{CO_2} is the total amount of moles of CO₂ converted in products. Since the stoichiometric coefficients of the carbon dioxide and of the product are the same, and the only source of carbon is represented by the CO₂, it can be assumed that the moles of CO₂ converted are equal to the moles of product synthesised. $E_{absorbed}$ represents the total energy absorbed by the PtX during the simulated period.

The results are reported in *Table 6.7*. It has to be remembered that the analysis performed is affected by the working conditions of the plants and the different final values of the storage levels. The latter accounts on the final value of energy absorbed, but it does not

distinguish the consumption related to the hydrogen production and the one for the final product synthesis.

Examining the PtX results individually, the Power-to-Methanol technology shows the best results. In fact, this type of plant converts most of the CO₂ and, at the same time, has the average PtX energy consumption among the three models studied. The Power-to-Syngas is the worst option because, despite the total amount of product synthesised is the highest among the PtX considered, only one third of the syngas is represented by carbon-based molecules (carbon monoxide). So, the effective product that embeds the carbon coming from the CO₂ is lower than the one produced by the Power-to-Methanol plants. Moreover, the Power-to-Syngas plants show the highest value of energy absorbed. Regarding the Power-to-Methane plants, they are a trade between the other two technologies studied, and they show the lowest value of energy absorbed but, at the same time, also the lowest global product synthesis.

A further distinction can be found between the winter and summer scenarios. For the summer reference interval, the PtX efficiencies result higher than the ones of the winter period. The reason is that during the summer, the FPPs work more than in winter, guaranteeing a higher production of methane, syngas, and methanol. Higher products synthesis means higher CO₂ converted.

Table 6.7 PtX converted CO₂ for both the PV share and the simulation periods

Reference period	Simulation settings	CO ₂ embedded,	CO ₂ embedded,
		30% PV (kgCO ₂ /MWh)	50% PV (kgCO ₂ /MWh)
Winter	Power-to-Methane	91.28	98.91
	Power-to-Syngas	88.29	99.00
	Power-to-Methanol	106.47	114.21
Summer	Power-to-Methane	102.24	101.57
	Power-to-Syngas	101.03	100.21
	Power-to-Methanol	117.28	116.17

7. Future studies

The main advantage related to the model built is the possibility to use it as a starting base case for future studies. Indeed, changing the input parameters several scenarios can be simulated. In my opinion, the functioning of the PtX plants on a year reference period should be the first thing to be better investigated. In fact, the outcomes of these simulations will give accurate information on the average working conditions of the plants and on its impact on the grid functioning. Additionally, a larger simulation interval also shows more reliable outcomes that could be used for a possible economic analysis of the plants.

The second interesting aspect that can be analysed in depth is the generation profile given as input at the model. It would be useful to consider the short and long terms future generation profiles that will more and more shaped by the RES generations. This kind of analysis enables to get useful information on the grid status and its negative phenomenon, both without and with the PtX plants installation. At the same way, the impact of the PtX plants on a grid supplied by several RES sources could be studied. For instance, it can be assumed that a PV generation would enhance the grid benefits of the PtX installation, but it represents a limit for the capacity factor of the plants since it restricts the functioning during the sunny days. Instead, since a wind generation profile is smooth and constant, it would show fewer grid issues and higher plants capacity factor.

A third future analysis that could be noteworthy to perform is related to an optimisation study. Starting from a defined scenario, where the number of PtX simulated, the installation nodes and the plants size are fixed, it would be useful to find the combination of the three different PtX plants which optimise an objective function. The objective function should take into account the results of the simulations as the reverse power flow reduction, the energy losses, and the capacity factors. Other factors can be also included as decision variables, like economic indexes. As seen from the results in Chapter 6, there is not any type of PtX plants that optimise all the outcomes evaluated; for this reason, a combination among them should represent a trade maximising the objective function.

The optimisation could be done by applying a genetic algorithm. The first step is to create a random initial population, intended as a series of vectors representing several combinations of the three PtX modelled. At each step, the algorithm evaluates the objective

function score, called fitness value, of each combination (individual) and then creates the next population. To create the next population for the successive algorithm step, three tasks have to be implemented:

- To sort the individuals by their fitness scores.
- To pass the individuals with the highest fitness score, known as elite, directly to the next generation.
- To obtain the remaining part of the population by making random changes to a single individual (mutation) or by combining the ‘genes’ of a pair of individuals (crossover).

Therefore, the algorithm replaces the current population with the individuals of the next generation. It stops when one of the stopping criteria is met. The main stopping criteria are represented by a maximum number of iterations, or a maximum elapsed time or when a fitness value is achieved [46].

8. Conclusion

This dissertation aims at evaluating the impact of the PtX plants installation on a distribution electric grid. The research shows the modelling of the entire process chain of three different PtX plants (methane, syngas and methanol), and their integration on a MV distribution semi-urban electric grid in different scenarios.

The various scenarios have been obtained diversifying both the simulated period (winter and summer) and the PV penetration factor (30% and 50%). For each scenario, three simulations were demonstrated, one for each modelled PtX type.

From the outcomes analysis results that the RPF, the most relevant parameter in this study, is reduced or completely removed by the three PtX installations. In the scenario with a PV share of 30%, the RPF is almost extinct (reduction of 98-100%). In the scenario with higher PV penetration, the RPF phenomenon is reduced of 58-96%. The RPF achieved are advantageous with major benefits for the winter simulation period.

Furthermore, the installation of PtX plants seems favourable because they allow the reduction of grid losses (-15% and -47%). The only case in which a slight increase of the losses (1-3%) is visible is represented by the low PV penetration winter scenario. As a matter of facts, the installation of further loads (PtX) on an already 'overloaded' grid leads to negative effects.

In addition, in all the simulated scenarios, the nodal voltages of the grid are always within the limits set by the regulation CEI EN 50160, while, regarding the overloading, the currents do not exceed the limits for the simulations with low PV penetration. Conversely, for the other PV penetration, the problem exists, especially during the summer period.

As of the PtX capacity factors that offer an estimate on how much the potential of the plants is exploited, these vary in a wide range. The main limit found in the study is linked to the scarce use of the plants in the winter period with low PV share, minimum average values of 14-15%. Both in the summer period with low penetration and in the ones simulated at high penetration, the average capacity factor values are satisfying (75%). The plant with the highest average capacity factors is the one producing syngas.

Besides, from the obtained results, the efficiency of each PtX installed was evaluated. In general, in the different operating conditions simulated, the efficacy of the plants is acceptable. In particular, for the Power-to-Methane plant, its efficiency varies between 44 and 54%, for the Power-to-Syngas plant between 42% and 51%, and for the Power-to-Methanol plant between 39% and 48%.

From the environmental point of view, the parameter that quantifies the functioning of the PtX plants is the CO₂ embodied in the three different products per unit of absorbed energy. The highest values are obtained by the Power-to-Methanol plants, varying between 107-118 kgCO₂/MWh. Then the Power-to-Methane with values between 92-103 kgCO₂/MWh, and in the end, the Power-to-Syngas between 89-101 kgCO₂/MWh.

To conclude, in general, the installation of the PtX plants on the grid studied brought utility and benefits, especially regarding the reduction of the reverse power flow phenomenon. Thus, these plant categories can be taken into consideration for the future to enable the ever greater spread of renewable intermittent plants, diminishing the unwanted effects on the electric grid.

Appendix

Appendix A - CO₂ Capture plant

MEA absorption-based plants are one of the most employed technologies in the post-combustion CO₂ capture. These kinds of plant can deal with a wide concentration of carbon dioxide in the stream treated. In *Table A.1*, some CO₂ concentrations of flue gases from different sources are reported.

Table A.1 CO₂ concentrations of several flue gases [47] [48]

CO ₂ gas source	CO ₂ molar concentration (%)
Aluminium Production	1-2
Natural Gas Combined Cycle	3-4
Conventional Coal fired Power Generation	13-15
Cement Production	14-33
Steel Production (blast furnace)	20-27
Integrated Gasification Combined Cycle	8-20
Biogas plant	25-45

Despite the wide operating conditions of chemical absorption technologies, these plants show an energetic drawback. The high reactivity of the MEA with the CO₂ molecules is an advantage in the absorption section, allowing to reach absorption efficiency higher than 90% [49], while it is a drawback in the desorption step. Indeed, a large energetic consumption is needed to break the bounds between MEA and CO₂. It is estimated that around the 80% of the heat requested by the CC plant is due to the regeneration of the MEA (pre-heating and re-boiling) [50].

The MEA carbon capture process consists of a first step where the flue gas ‘rich’ in CO₂ is sent in the bottom of an absorption column, while the cold lean MEA enters from the top. The counter-current flow of the two streams enhances the contact area between flue gas and MEA, guaranteeing a high CO₂ absorption. At the top of the absorber, the stream is cooled. The condensed phase represented by the aqueous MEA solution is sent back to the top of the absorber, while the not condensed one (clean flue gas) exits the CC plant. At the bottom

of the absorber, the cold rich MEA is collected and then pumped through a heat exchanger where it is pre-heated. Then the hot rich MEA enters at the top of a stripping column where it is further heated up with a steam flow. The increase of temperature allows the desorption process of the CO₂ that is conveyed to the top of the column. Here, the residual MEA is condensed and separated from the gaseous CO₂. MEA is sent back to the top of the stripping column, while the CO₂ is sent to the compression stages. At the bottom of the column, the hot lean MEA is heated up and separated from the produced steam. The hot lean MEA is sent to the heat exchanger transferring heat to the cold rich MEA stream. Hence, the cold lean MEA is further cooled before being sent to the top of the absorber column. The cycle starts again as shown in *Figure A.1*.

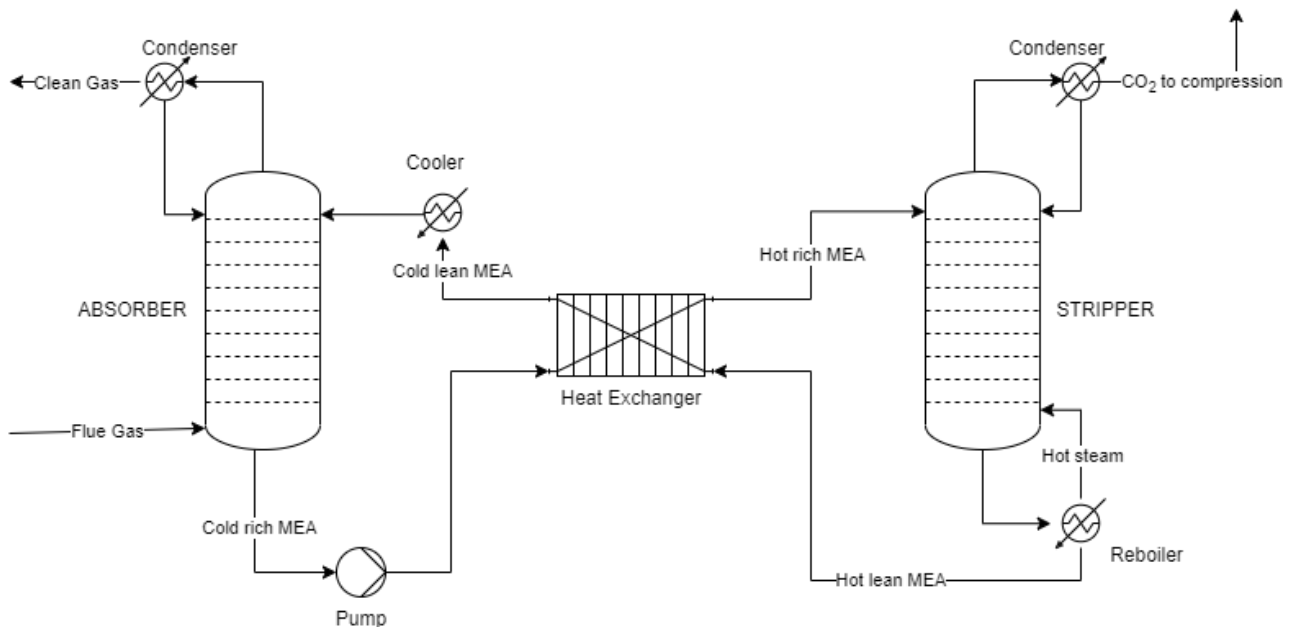


Figure A.1 CO₂ capture plant with MEA

Appendix B – MATLAB code description

The developed MATLAB code can be schematised in four sections:

- Initialization. The first part of the code is represented by the definition of the electric grid parameters, like branches length and impedance, loads and generations profile.

Furthermore, the PtX model parameters and the strategy thresholds are loaded in the workspace environment through the definition of MATLAB structure (*Table A.2*). The number of Power-to-X plants installed, the typology and their size are other input parameters set in this section.

To conclude, the Backward and Forward Sweep algorithm is run to evaluate the initial nodes voltages and branches current.

- PtX model. Then inside the two ‘for cycles’, where the external one increases the timestep of the simulation and the internal switches the number of plants installed, the PtX function is run. The input parameters needed by the function are:
 - The net power surplus defined for the PtX installation node and the timestep.
 - The type of PtX considered among the methanation, syngas synthesis and methanol synthesis.
 - The size of PtX electrolyser installed.
 - The hydrogen storage level at the previous timestep for each PtX installed.
 - The FPP status at the previous timestep for each PtX installed.
 - A variable storage threshold at the previous timestep for each PtX installed for the implementation of the strategy.
- Output calculation and results. In this last section, the output of the PtX function are saved and a new Backward and Forward Sweep cycle is run to evaluate the new grid status. Then from the outputs, the reverse power flow, the other grid issues, and the power losses can be detected. Also, the capacity factor of each PtX can be calculated.

A simplified scheme of the model is show in *Figure A.2*.

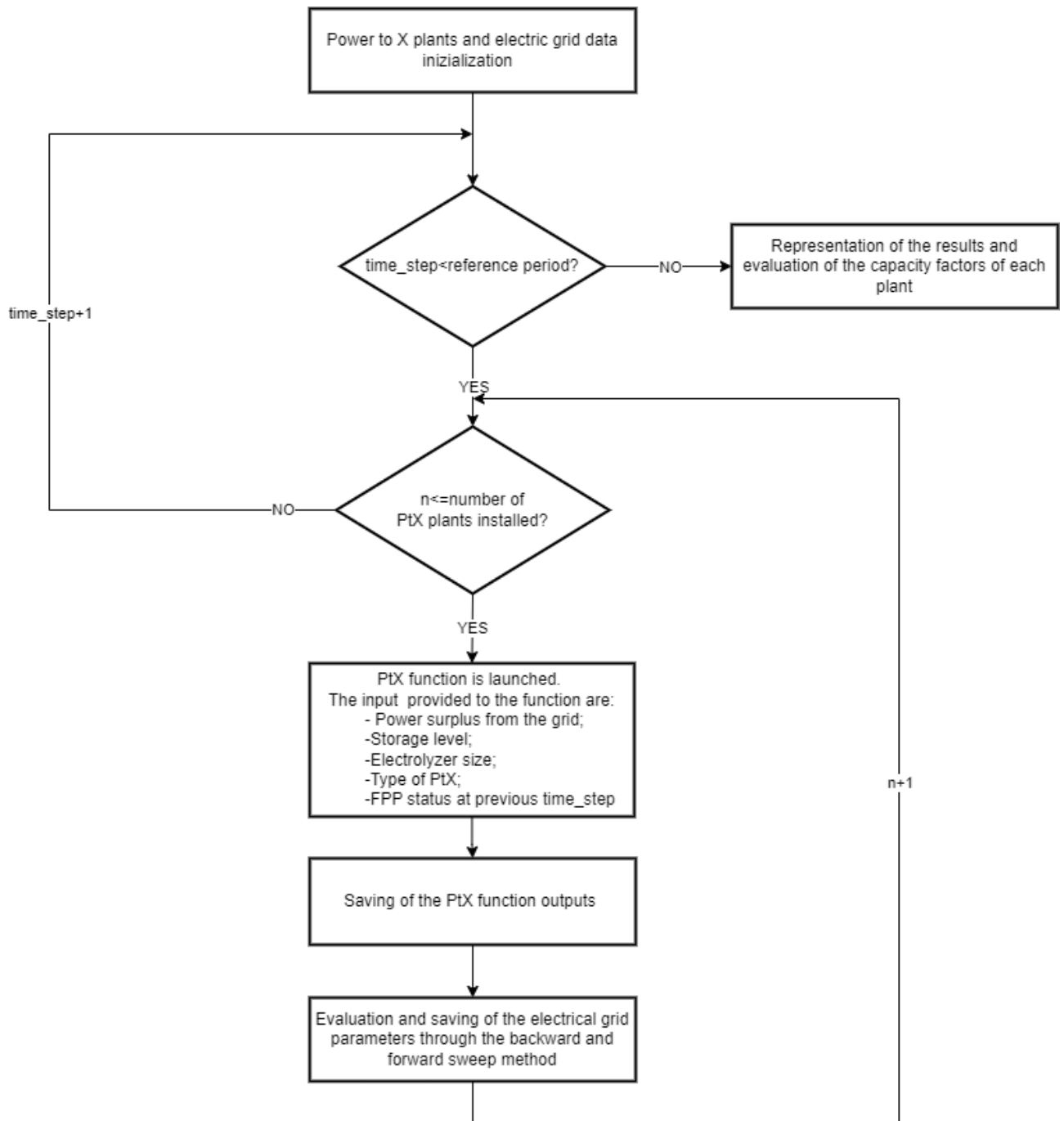


Figure A.2 Block diagram of algorithm implemented through the MATLAB code

For the sake of completeness, the strategy parameters implemented in the simulation are reported in *Table A.2*.

Table A.2 Strategy parameters of the model

Parameters	Description	Value
Initial storage (-)	Initialization of the hydrogen storage level	0.5
Autonomy (s)	Hydrogen storage autonomy	54000
Max storage (-)	Maximum storage level, the additional hydrogen cannot be stored	1
Min storage (-)	Minimum storage level, hydrogen cannot be drawn anymore	0.1
FPP threshold (-)	Minimum storage level to be satisfied for allow to work the FPP when there is no power surplus	0.9
FPP on (-)	ON status of the FPP	1
FPP off (-)	OFF status of the FPP	0
Compr on (-)	ON status of the hydrogen compressors	1
Compr off (-)	OFF status of the hydrogen compressors	0
FPP capacity (-)	Minimum power capacity at which the FPP could work	0.35
Tolerance (-)	Stopping threshold for the for cycle that equalise the power absorbed by the PtX and the surplus power from the grid	0.0001

References

- [1] “EDGAR - The Emissions Database for Global Atmospheric Research.” <https://edgar.jrc.ec.europa.eu/> (accessed Feb. 12, 2023).
- [2] D. Romano, “ L’andamento delle emissioni nazionali di gas serra ISPRA-Istituto Superiore per la Protezione e la Ricerca Ambientale,” 2021.
- [3] “Emissioni di gas serra per paese e settore: Infografica | Attualità | Parlamento europeo.” <https://www.europarl.europa.eu/news/it/headlines/society/20180301STO98928/emissioni-di-gas-serra-per-paese-e-settore-infografica> (accessed Mar. 13, 2023).
- [4] “KYOTO PROTOCOL TO THE UNITED NATIONS FRAMEWORK CONVENTION ON CLIMATE CHANGE UNITED NATIONS,” 1998.
- [5] Unfccc, “ADOPTION OF THE PARIS AGREEMENT - Paris Agreement text English,” 2015.
- [6] G. Erbach, L. Jensen, S. Chahri, and E. Claros, “Fit for 55 package - Towards climate neutrality,” Jun. 2022.
- [7] “Statistics | Eurostat.” https://ec.europa.eu/eurostat/databrowser/view/NRG_IND_REN__custom_4832133/default/table?lang=en (accessed Feb. 12, 2023).
- [8] T. International Renewable Energy Agency, *GREEN HYDROGEN COST REDUCTION SCALING UP ELECTROLYSERS TO MEET THE 1.5°C CLIMATE GOAL H 2 O 2*. 2020. [Online]. Available: www.irena.org/publications
- [9] “Round Trip Efficiency | energymag.” <https://energymag.net/round-trip-efficiency/> (accessed Mar. 08, 2023).
- [10] G. Prettico, F. Gangale, A. Mengolini, A. Lacas, and G. Fulli, “From European Electricity Distribution Systems to Representative Distribution Networks,” 2016.
- [11] C. Mateo Domingo, T. Gómez San Román, Á. Sánchez-Miralles, J. P. Peco González, and A. Candela Martínez, “A reference network model for large-scale

- distribution planning with automatic street map generation,” *IEEE Transactions on Power Systems*, vol. 26, no. 1, pp. 190–197, Feb. 2011, doi: 10.1109/TPWRS.2010.2052077.
- [12] L. Serra, A. Mazza, E. Bompard, and E. Pons, “Analisi dell’impatto della tecnologia Power-to-Gas sull’esercizio di reti di distribuzione con elevata penetrazione di risorse rinnovabili,” 2018.
- [13] “Solar PV installation cost worldwide 2021 | Statista.” <https://www.statista.com/statistics/809796/global-solar-power-installation-cost-per-kilowatt/> (accessed Mar. 09, 2023).
- [14] “Global LCOE and Auction values.” <https://www.irena.org/Data/View-data-by-topic/Costs/Global-LCOE-and-Auction-values> (accessed Mar. 09, 2023).
- [15] “Renewable electricity – Renewable Energy Market Update - May 2022 – Analysis - IEA.” <https://www.iea.org/reports/renewable-energy-market-update-may-2022/renewable-electricity> (accessed Mar. 09, 2023).
- [16] “Renewable Electricity – Analysis - IEA.” <https://www.iea.org/reports/renewable-electricity> (accessed Mar. 09, 2023).
- [17] “The Bright Solar Model .” <https://jamiembright.github.io/BrightSolarModel/> (accessed Feb. 12, 2023).
- [18] “JRC Photovoltaic Geographical Information System (PVGIS) - European Commission.” https://re.jrc.ec.europa.eu/pvg_tools/en/ (accessed Feb. 12, 2023).
- [19] “Norma Italiana CEI - Regola tecnica di riferimento per la connessione di Utenti attivi e passivi alle reti AT e MT delle imprese distributrici di energia elettrica,” 2012.
- [20] R. Li and C. Li, “Photocatalytic Water Splitting on Semiconductor-Based Photocatalysts,” *Advances in Catalysis*, vol. 60, pp. 1–57, Jan. 2017, doi: 10.1016/BS.ACAT.2017.09.001.
- [21] M. Santarelli, “Celle a combustibile a membrana polimerica Modello elettrochimico Polygeneration and advanced energy systems CELLE A COMBUSTIBILE A MEMBRANA POLIMERICA. MODELLO ELETTROCHIMICO.”

- [22] I. S. Martín, A. Ursúa, and P. Sanchis, “Modelling of PEM fuel cell performance: Steady-state and dynamic experimental validation,” *Energies (Basel)*, vol. 7, no. 2, pp. 670–700, 2014, doi: 10.3390/en7020670.
- [23] “Combustibili - Potere calorifico Inferiore ”, Accessed: Mar. 03, 2023. [Online]. Available: <https://www.docenti.unina.it/webdocenti-be/allegati/materiale-didattico/258681>
- [24] R. K. Sinnott, “Coulson & Richardson’s Chemical Engineering Design, 4th ed., vol. 6,” Oxford, 2005.
- [25] “Peat | Description, Formation, Importance, Carbon, & Uses | Britannica.” <https://www.britannica.com/technology/peat> (accessed Mar. 07, 2023).
- [26] “European Commission - Methane emissions.” https://energy.ec.europa.eu/topics/oil-gas-and-coal/methane-emissions_en (accessed Mar. 07, 2023).
- [27] “Supply – Key World Energy Statistics 2021 – Analysis - IEA.” <https://www.iea.org/reports/key-world-energy-statistics-2021/supply> (accessed Mar. 07, 2023).
- [28] F. Salomone, E. Giglio, D. Ferrero, M. Santarelli, R. Pirone, and S. Bensaid, “Techno-economic modelling of a Power-to-Gas system based on SOEC electrolysis and CO₂ methanation in a RES-based electric grid,” *Chemical Engineering Journal*, vol. 377, Dec. 2019, doi: 10.1016/j.cej.2018.10.170.
- [29] H. Er-rbib and C. Bouallou, “Modeling and simulation of CO methanation process for renewable electricity storage,” *Energy*, vol. 75, pp. 81–88, Oct. 2014, doi: 10.1016/j.energy.2014.05.115.
- [30] G. Calì, E. Loria, C. Frau, P. Miraglia, D. Multineddu, and A. F. Orsini Tedde, “Test di separazione della CO₂ da syngas presso impianto pilota MINISTERO DELLO SVILUPPO ECONOMICO,” 2014.
- [31] D. W. Green and R. H. Perry, “Perry’s Chemical Engineers’ Handbook,” 2008.

- [32] “Compressibility Factor, Z Factor - Engineering Units.” <https://engineeringunits.com/compressibility-factor-z-factor/> (accessed Feb. 14, 2023).
- [33] “Legge di van der Waals - Wikipedia.” https://it.wikipedia.org/wiki/Legge_di_van_der_Waals (accessed Feb. 12, 2023).
- [34] “NIST Chemistry WebBook.” <https://webbook.nist.gov/chemistry/> (accessed Feb. 12, 2023).
- [35] “TMR Cooling towers with centrifugal fans.” Accessed: Feb. 13, 2023. [Online]. Available: https://uploads-ssl.webflow.com/608a7afa4bc0372c48e8fa8b/6246d4cecb79426e4e1622fa_catalogue-TMR-03-22-2.pdf
- [36] “Metanolo - Chimica Industriale Essenziale .” <https://www.chimicaindustrialeessenziale.org/prodotti-chimici-di-base/metanolo/> (accessed Mar. 07, 2023).
- [37] SGS INSPIRE team, “METHANOL: PROPERTIES AND USES,” 2020.
- [38] “Metanolo da CO₂: applicazioni e prospettive - Sotacarbo SpA | Ricerca e sviluppo di Energie pulite.” <https://www.sotacarbo.it/it/2020/05/metanolo-da-co2-applicazioni-e-prospettive/> (accessed Mar. 07, 2023).
- [39] A. A. Kiss, J. J. Pragt, H. J. Vos, G. Bargeman, and M. T. de Groot, “Novel efficient process for methanol synthesis by CO₂ hydrogenation,” *Chemical Engineering Journal*, vol. 284, pp. 260–269, Jan. 2016, doi: 10.1016/j.cej.2015.08.101.
- [40] Y. Cao *et al.*, “Synthesis gas production with an adjustable H₂/CO ratio through the coal gasification process: Effects of coal ranks and methane addition,” *Energy and Fuels*, vol. 22, no. 3, pp. 1720–1730, May 2008, doi: 10.1021/ef7005707.
- [41] R. Ahmed El-Nagar and A. A. Ghanem, “Syngas Production, Properties, and Its Importance,” 2019, doi: 10.5772/intechopen.89379.
- [42] J. A. Díaz *et al.*, “Cobalt and iron supported on carbon nanofibers as catalysts for Fischer–Tropsch synthesis,” *Fuel Processing Technology*, vol. 128, pp. 417–424, Dec. 2014, doi: 10.1016/J.FUPROC.2014.08.005.

- [43] M. González-Castaño, B. Dorneanu, and H. Arellano-García, “The reverse water gas shift reaction: A process systems engineering perspective,” *Reaction Chemistry and Engineering*, vol. 6, no. 6. Royal Society of Chemistry, pp. 954–976, Jun. 01, 2021. doi: 10.1039/d0re00478b.
- [44] “Tabella potere calorifico di vari combustibili.” <https://www.ingdemurtas.it/tabelle/potere-calorifico/> (accessed Mar. 03, 2023).
- [45] “Carbon monoxide properties.” http://gruppo-hera.it/documenti/note_tecniche/OSSIDO%20DI%20CARBONIO.pdf (accessed Mar. 03, 2023).
- [46] “Genetic Algorithm - MATLAB & Simulink.” <https://it.mathworks.com/discovery/genetic-algorithm.html> (accessed Mar. 04, 2023).
- [47] A. Vita, M. lo Faro, M. Laganà, M. Minutoli, L. Pino, and A. Aricò, “Biogas: un’opportunità per le SOFC - CNR - Istituto di Tecnologie Avanzate per l’Energia ‘Nicola Giordano’ Messina,” 2012.
- [48] J. Husebye, A. L. Brunsvold, S. Roussanaly, and X. Zhang, “Techno Economic Evaluation of Amine based CO₂ Capture: Impact of CO₂ Concentration and Steam Supply,” *Energy Procedia*, vol. 23, pp. 381–390, Jan. 2012, doi: 10.1016/J.EGYPRO.2012.06.053.
- [49] F. Barzagli, F. Mani, and M. Peruzzini, “A Comparative Study of the CO₂ Absorption in Some Solvent-Free Alkanolamines and in Aqueous Monoethanolamine (MEA),” *Environ Sci Technol*, vol. 50, no. 13, pp. 7239–7246, Jul. 2016, doi: 10.1021/ACS.EST.6B00150.
- [50] J. Jung, Y. S. Jeong, Y. Lim, C. S. Lee, and C. Han, “Advanced CO₂ capture process using MEA scrubbing: Configuration of a split flow and phase separation heat exchanger,” *Energy Procedia*, vol. 37, pp. 1778–1784, 2013, doi: 10.1016/J.EGYPRO.2013.06.054.

Acknowledgements

I end this hard and challenging part of my life, and it is time to thank many people that helped me during these years.

Firstly, I would like to thank the Professor Pirone and the tutors Ing. Mazza and Ing. Salomone for the opportunity of working on this thought-provoking topic and, especially, for the patience and the support they gave me.

A huge thanks to my parents, my brother and to all my family that allowed me to pursue this career and reassured me during all the tough moments.

Thanks to my girlfriend Jacqueline, always available to support me during this stressful period and for the fundamental help with the dissertation.

To conclude I would like to thank all my friends, Andrea, Marco, Raffaele, Massimo, Matteo, Mirko, and the others who I am not mentioning. And my relatives based in Turin for the delightful moments shared.